INTERPLAY BETWEEN SHAPE, ORDER AND TOPOLOGICAL DEFECTS: *ELASTICITY OF SOME SOFT CONDENSED MATTER SYSTEMS*

JAYA KUMAR. A

Raman Research Institute
Bangalore

Thesis submitted to the Jawaharlal Nehru University for the degree of
Doctor of Philosophy

August 2014

Jaya Kumar. A: *Interplay between shape, order and topological defects: Elasticity of some soft condensed matter systems,* A study on geometry and topology in soft condensed matter systems, © August 2014

DECLARATION

I, hereby, declare that this thesis is composed independently by me at Raman Research Institute, Bangalore, India, under the supervision of Prof. Yashodhan Hatwalne. The subject matter presented in this thesis has not previously formed the basis of the award of any degree, diploma, associateship, fellowship or any other similar title in any other University.

Prof. Yashodhan Hatwalne
(Thesis supervisor)
Raman Research Institute

Jaya Kumar. A

CERTIFICATE

This is to certify that the thesis entitled **Interplay between shape, order and topological defects: Elasticity of some soft condensed matter systems** submitted by Jaya Kumar A. for the award of the degree of DOCTOR OF PHILOSOPHY of Jawaharlal Nehru University is his original work. This has not been published or submitted to any other University for any other degree or diploma.

Dr. Ravi Subramaniam
Director
Raman Research Institute

Dr. Yashodhan Hatwalne
Thesis supervisor

Dedicated to my parents and teachers.

SYNOPSIS

In this thesis, we study the interplay between shape, order and topological defects in two-dimensional soft condensed matter systems. Curvature and topological defects introduce geometrical frustrations in order. The strength of interactions, type and number of defects, and the ground state that we start with impact the nature of frustration. Different aspects of this problem are addressed in the thesis. Motivation and results for each chapter are highlighted as follows :

Equilibrium of fluid membranes with tangent-plane order:

A two dimensional fluid membrane can have tangent-plane order such as hexatic, nematic, tilt(vector) etc. When these membranes bend the geometry induces distortions in the tangent-plane order leading to geometric frustration.

In this chapter, we analyze the coupling between shape and order in simplest model of fluid membrane with vector or nematic order. The formulation we choose to analyze directly brings out the connection between shape of the membrane and topology of the field embedded on the membrane. The shape and tangent-plane order field are varied independently to derive the equations of equilibrium together with the boundary conditions. The formulation developed, which is traditionally used in the context of membranes can also be applied to liquid crystals such as Sm-C, Sm-C* etc. We are in the process of applying this formulation to consider dispirations in Sm-C*.

Classification of 2D crystal ground states:

A carbon nanotube can be made by rolling graphene sheets into cylinders of ~ 1 nanometer diameter. Due to hexagonal symmetry of graphene, one can choose a range of rolling directions with respect to basis vectors of its lattice. This gives rise to different ground states. Experimental and theoretical analysis show that the mechanical and electronic properties of the nanotubes change drastically with the rolling direction. In addition to tubular structures, carbon nanotori have been observed experimentally and show high paramagnetic moments. This paramagnetic moment has been shown to depend critically on the crystalline structure. Thus, there is a need to characterize and classify the different ground states of 2D crystals.

In this chapter, we study the different ground states of crystalline order on a closed, compact surface of any genus without boundaries. In literature homotopy theory has been used to classify the ground states of ordered media in presence of defects. But for systems with discrete translational symmetry homotopy theory leads to results which are incorrect, such as existence of $+2$ charge disclination. We adopt foliation theory from the study of dynamical systems to classify the ground states of 2D crystals using ribbon graphs, called separatrix, which decomposes a surface with crystalline order into cylinders. The separatrix also provides a mechanism by which one can generate a class of distinct ground states. Using the separatrix we classify ground states of closed compact surfaces with crystalline order having half-integer strength disclinations and dislocations.

Phenomenology of tent morphologies of polymer crystallites: There is a significant difference between the growth of atomic crystals and polymeric crystals. Polymeric crystals have connectedness. This leads to interesting consequences regarding the shape and morphology of polymer crystals. All the observed morphologies of polymer crystallites are lamellar in nature. These either show spherulitic structures composed of helicoids, or tent-like structures or scroll structures.

In this chapter, we focus on the tent morphology of polymer crystallites and suggest arguments to explain the stability of this morphology. Here, we attempt to solve the problem of why a crystallite should buckle into the form of a tent using some simple notions from soft condensed matter and geometry. We propose that polymer folds are responsible for the 3D structure of tent morphology. A phenomenological model is formulated in which anisotropic line tension, due to folds, help trap a disclination in the fold field. We obtain an exact solution for two orthogonal solitons in 2D which satisfy the equations of equilibrium and the corresponding boundary conditions. The solitons split the crystal into sectors with uniformly oriented folds in each sector. Further, the crystal lamella is buckled into the tent structure by a sliding mechanism such that the crystal order within the finite thickness of the lamella is free of any topological defects.

Prof. Yashodhan Hatwalne	**Jaya Kumar. A**
(Thesis supervisor)	
Raman Research Institute	

ACKNOWLEDGEMENTS

It was a pleasure working with Yashodhan. His old school, laid back approach to physics is exactly how I fantasized physicists would be. An endangered class of physicist. I am grateful to Yashodhan for letting me explore the field on my own and not imposing any time-constraints. He never stops to surprise me with his deep insights into the problems we work on. Lucky to have a guide who can cook dinner. Thank you Swati for the tasty food and your regular caring concerns regarding my work and life at RRI.

I am indebted to Muthu for technical and moral support. I thank Muthu and Yashodhan for the wonderful problem on polymer crystals which formed the genesis for all the work related to the thesis. I have learnt a lot from my intermittent interactions with Sam, Madan, Raghu and Madhusudana. Raghu, as SAAC was instruemental in getting my thesis through on time.

My long stay at RRI was a breeze thanks to RK and Madhukar. Hats off to you guys for all binge on acamedic and non-academic activities. Maddy gave us hope and reassurance that age is just a number. I am going to badly miss the tea and coffee sessions with Mari and Swami. Nagu, Wasim, Ravi, Nandan, Arijit, Chaitra, Giri, Katti, Nishant, Chandra, Prakhyat, Chandan, Jaggu, Avinash, Kripa, Venu, Venkat, GB : life wouldn't be the same without you guys.

RRI gave me ample opportunities to hone my skills in shuttle, football, volleyball and cricket. Sports kept my evenings entertained and formed the spring boards for the night-outs. I am fortunate to have been part of groups involved in organizng various events at RRI.

Thanks to Krishna, I have managed to scrape through most of the administrative requirements. Manju, krk and Marisa have been helpful in times of need. Library was my cocoon where I could recuperate from any setbacks I had in my work. I thank the library staff for their organized services.

Last but not least thanks to my parents for the unrelenting support and always questioning my choices. I cannot think of a logical reason why any parents would do this.

It was a joyride, which fittingly ended with this wild roller coaster ride in last few weeks.

CONTENTS

1 INTRODUCTION 1
- 1.1 Symmetry and order 1
  - 1.1.1 Curvature 2
  - 1.1.2 Order 2
  - 1.1.3 Order + Curvature = Frustration 3
- 1.2 Defects 4
  - 1.2.1 Order + Defect = Curvature 5
  - 1.2.2 Order + Curvature = Defect 6
- 1.3 Classification: Defect = Curvature 6
- 1.4 Polymer crystal 6

2 EQUILIBRIUM OF FLUID MEMBRANES WITH TANGENT-PLANE ORDER 9
- 2.1 Elastic Free energy of fluid membranes 9
- 2.2 Elastic free energy of fluid membranes with tangent-plane order 10
  - 2.2.1 Flat membrane (freeze the bending degree of freedom) 10
- 2.3 Coulomb gas model 15

Appendices 17

A DIFFERENTIAL GEOMETRY 19
- A.1 Derivation of the covariant version in terms of θ 19
- A.2 Anti-symmetric tensor 22

3 CLASSIFICATION OF 2D CRYSTAL GROUND STATES 23
- 3.1 Crystalline order on a surface 27
- 3.2 Gift wrapping problem 27
  - 3.2.1 Case study: Torus $\mathrm{MCG}(\mathbb{T}^2)$ 31
  - 3.2.2 Higher genus compact, closed, orientable surfaces 33
  - 3.2.3 Need for finer structure/classification 34
- 3.3 Flat surfaces 35
  - 3.3.1 Translation surfaces 37
  - 3.3.2 Decomposition of the translation surface into cylinders: Separatrix diagram 39
- 3.4 Inclusion of half-integer strength topological defects 44

4 PHENOMENOLOGY OF TENT MORPHOLOGIES OF POLYMER CRYSTALLITES 49
- 4.1 Experimental facts: 49
- 4.2 Phenomenological model of polymer crystallites 51
  - 4.2.1 Formation of sectors 53
  - 4.2.2 Buckling of polymer crystal lamella 55

Appendices 59

B ADDENDUM TO CHAPTER 4 61

B.1 Coupling between fold/tilt and curvature 61

BIBLIOGRAPHY 65

LIST OF FIGURES

Figure 1 Parametrization of a surface. 2

Figure 2 Top: Cylinder is cut open along the axis and flattened to a plane to mark the constant vectors. Now if the cylinder is glued back together and cut in any direction to flatten, the vectors still preserve the directions. Bottom: A cube is opened up and flattened. Constant vectors marked and glued back together. Now if the cube is opened up by cutting along different sets of edges, you find that on flattening vector could change direction. This happens because cube has Gaussian curvature at each corners, where as the cylinder has zero Gaussian curvature. 3

Figure 3 Two different tilings of a plane by pentagons wth gaps. 4

Figure 4 A disclination is obtained by removing or inserting a sector from/into the membrane. In 2D a dislocation can be modeled as a disclination pair (remove and insert back a sector with some translation). 5

Figure 5 (a) Buckled positive disclination. (b) Buckled negative disclination. 5

Figure 6 (a) Buckled dislocation pair. (b) Buckled small angle grain boundary, modeled as an array of dislocation pairs. 6

Figure 7 (a) AFM topographic image showing the 3D structure of tent morphology of polyethylene crystal, and (b) is the height field along the line shown in (a). (c) Schematic of the tent structure. 7

Figure 8 Darboux frame $\left\{\hat{\mathbf{t}}_{(b)}, \hat{\mathbf{n}}, \hat{\mathbf{n}}_{(b)}\right\}$ for a membrane with boundary. 13

Figure 9 Lie dragging the $\hat{m}$ - field. 13

Figure 10 Based on the rolling direction of graphene, the nano tubes are classified as, A: Arm chair, B: Zig-Zag, C: Chiral. 23

Figure 11 High genus fullerenes with heptagons and hexagons (no pentagons) holey balls. (a) Two-fold axis of a 2040-atom genus 11 fullerene. (b) Five-fold axis. (c) Cut perpendicular to the five-fold axis. (d) A genus 5 holey ball with 1896 atoms. 24
Figure 12 A circle can be made straight (geodesic), such that its curvature w.r.t. the surface it is sitting in (geodesic curvature) is zero, by embedding the circle on a cylinder as shown in the left. Similarly a flat (zero Gaussian curvature) torus can be obtained by embedding a flat cylinder in a 3d box, such that the open ends of the cylinder lie on opposite faces of the box as shown in the right figure. And then the opposite faces of the box are identified without stretching in 4d. On identification of the opposite faces, the cylinder becomes a torus. Notice that as in the case of the circle, the torus is flat w.r.t. the box. 24
Figure 13 Chocolate-glazed doughnuts: Two different covers of a torus, of the same geometry that are not deformable into each other, which are not deformable to each other. With the loop formed by the boundary of chocolate representing a coordinate axis, the two tori have different winding numbers. 24
Figure 14 Volterra construction in 3d: The figure demonstrates the effect of defects presence on concentric cylindrical sections of the medium. The coordinate system on the top-left of each configuration indicates the action on the lower cut face. 26
Figure 15 Volterra construction in 2d: Figure on left is the construction of a disclination and the one on right is a dislocation formed by a pair of equal and opposite disclinations. 26
Figure 16 17 possible wallpaper groups 28
Figure 17 The wrapping problem. 28
Figure 18 Schematic of wrapping rules: 29
Figure 19 Figure shows how three patches of wrapping paper can be glued together such that the pattern is seamless and leaves a pin hole at the point of intesection of boundaries of all three patches. The pinhole left is the core of a $+1/2$ disclination (π rotation). 29

Figure 20 Charts and maps on a surface with crystalline order. Here a part of the surface sitting in 3d is covered by two patches with square lattice symmetry and a transition map of rotation by $\frac{\pi}{2}$. 30

Figure 21 An orbifold formed by quotienting a plane by a discrete crystal point group is a cone. If the group is a reflection along a straight line, as in the right, then one gets a half plane with a boundary. The grey area in the plane has a one-to-one map to the orbifold. 30

Figure 22 Figure on the right shows the operation of Dehn twist on a cylindrical section. The effect on the winding number is shown in the left figure. Observe that there are no deformations at the boundaries. 31

Figure 23 Generation of different surfaces with crystalline order on a torus by Dehn twist. First column shows the vectors and the fundamental regions that form the torus. Last column shows the geometrically equivalent tori with different winding numbers. 32

Figure 24 Different class of surfaces are shown, only surfaces in the first row are analyzed below. 33

Figure 25 The figure at the top show separating curves. Bottom row shows the Lickorish generators for a surface without defects. 33

Figure 26 The three generating curves on a torus with two defects are shown. The corresponding case for a dislocation pair is discussed in sec. 3.4.0.1. 34

Figure 27 Comparison between full and partial Dehn twists 35

Figure 28 Problem with implementing partial Dehn twists: Since in the case of Dehn twists the boundary is not deformed the orientation of cut made to extract the cylindrical section doesn't matter. But for partial Dehn twist the cut has to be along the crystallographic axis. The cylindrical sections shown in the bottom row can undergo Dehn twists, but any partial twist will make them incompatible to insert back into the surface. 35

Figure 29 Flat surface and constant curvature surfaces form the extreme models analyzed in this chapter. Flat surfaces have planar faces, straight edges and isolated conical singular points and are ideal for studying the properties of geodesics. 36

Figure 30 To construct a cone out of paper, a sector of deficit angle α is removed and the cut edges glued together. Then the cone is flat, i.e. Gaussian curvature is zero, everywhere except the apex. 37
Figure 31 Construction of paths $\mathcal{P}$ and $\mathcal{P}'$ on the crystalline lattice with principal crystallographic axes along $\vec{a}$ and $\vec{b}$. The horizontal lines as well as the vertical lines of the lattice represent the geodesics. Here sum of all internal angles ϕ_i's equals $\pi(n-2)$, for an n-gon. Hence the total deficit angle and the integral of Gaussian curvature is -4π, implying it is a genus two surface by Gauss-Bonnet theorem (57). 38
Figure 32 First row shows the construction of a torus and a handle. Second row demonstrates the sequence of operations to build a genus 2 surface. Here the sides of an octagon (similar to the one of fig. 31) with identical markings are glued together. All vertices of the octagon meet at a defect point with disclination strength -1. The last row shows how a genus two surface can be cut open and flattened out into an octagon. 39
Figure 33 The exit and reemergence of horizontal lines (geodesics) into the polygon with identified (glued) edges. Being a translation surface, all geodesics continue to flow in the same direction. 39
Figure 34 The trace of a horizontal critical geodesic that starts from one vertex and ends at another. There are other critical geodesics. For example the horizontal geodesic begining at the origin. This particular geodesic starts at a vertex and directly ends at a vertex. Figure on the right shows the development of a critical geodesic into a ribbon. 40
Figure 35 The ribbons on a polygonal translation surface (torus) are marked. Edges with similar markings are glued together to get the actual surface with crystalline order. Then ribbon is cut out of the surface to get the separatrix. 41

Figure 36 Top row shows the alternate construction of separatrix for a torus. The grey regions in the patch are the ribbons, that are to be cut out and glued together. Though the two tori have different crystalline order (differs by a partial Dehn twist) the separatrix are the same. It needs a label to further distinguish them. Similar construction is carried out for a genus two surface in the second row. The polygonal translation surface at the bottom for the genus two surface is an octagon, with three vertices on the bottom edge (one is hidden). 42

Figure 37 Example to demonstrate the labeling: Separatrix for a genus two surface which differ by a partial Dehn twist are shown. The number in box for the separatrix are the label (width, height, twist of cylinderical sections). The calculation of twist is shown in the bottom-left figure. 43

Figure 38 Reconstruction of the actual surface with crystalline order from the separatrix, by attaching cylinders. There are four loops corresponding to the separatrix on the left. Based on the labels (width, height and twist of cylinder) on the loops, cylinders are attached to get the actual surface with crystalline order. In the first step the separatrix is represented by a disc with holes having boundaries C_2, C_3, C_4. The disc has a boundary C_1. In the second step C_3 and C_4 are connected by a cylinder, whose width, height and twist are given by the label on C_3 and C_4. Same procedure is implemented on C_1 and C_2 in the last step. 44

Figure 39 A torus is generated by two vectors. Disclinations are included into the torus by partitioning the horizontal vector into three vectors, $(\vec{B}, \vec{C}, \vec{D})$ and then replacing one of them, $\vec{C}$, by two vertical vectors, $(\vec{a}, \vec{b})$, and one horizontal vector, $\vec{c}$. Observe that the internal angle at the vertex corresponding to the starting point of $\vec{a}$ is $(\phi_1 + \phi_2) = \pi$, and hence a disclination of strength $+\frac{1}{2}$. The last figure shows how any vector can be decomposed into a horizontal and vertical vector, to implement the above operation of including defect. Using the above approach more defects can be introduced by partitioning horizontal vectors, $\vec{B}$, $\vec{D}$ or $\vec{c}$. 44

Figure 40 Schematic to demonstrate regions in a torus with defects where the geodesics change directions on crossing over an edge. First figure shows the reversal of geodesic direction on crossing $\vec{a}$ (sides of the polygon idenitified in the direction of the vector). Second figure shows that the geodesic direction is preserved on crossing $\vec{A}$. In the last figure, geodesic reverses direction on crossing $\vec{b}$. 45

Figure 41 Construction of separatrix for a torus with $\pm 1/2$ strength disclinations. In the first step the polygonal surface is cut along middle vector 7 and rearranged as in the second figure. Then the ribbons are marked, cut out and joined together to get the separatrix. The separatrix has two disconnected parts. 45

Figure 42 The disclinations in fig. 39 are transformed into dislocation by reducing magnitudes of $\vec{a}$ and $\vec{b}$ to half the lattice spacing, as in the second figure, and the vectors in this polygonal surface are scaled by 2 to get the third figure (i.e. $\vec{A}' = 2\vec{A}$ and so on). The corresponding sepratrix is shown in last figure. 46

Figure 43 The effect of partial Dehn twist on the torus with dislocation is the same as plastic deformation called dislocation glide shown in the last set of figures. 46

Figure 44 A tetrahedron with triangular lattice can be opened up into a parallelogram with the identifications shown. The thrid figure shows corresponding separatrix. The effect of applying partial Dehn twist is shown in the last figure. 47
Figure 45 A Rubik's cube is equivalent to a flat sphere with eight disclinations sitting at the corners. Partial rotations of a Rubik's cube can generate crystallographically distinct set of spheres. Figure on the extreme right shows the deformed cube. 47
Figure 46 The cube is opened up to give a flat surface. Notice that it is not a translation surface as any horizontal geodesic in the bottom section reemerges as a vertical geodesic (dotted line) on crossing an edge. If the vertical parts are left out of the separatrix construction one gets half ribbons as shown on the right. 48
Figure 47 Polyethylene mono-crystal decorated by vacuum deposition of polyethylene. Polyethylene stripes show the four crystal growth sectors.(Copyright : J. C. Wittmann, B. A. Lotz, ICS Strasbourg) 49
Figure 48 The crystal structure of polyethylene ($[CH_2 - CH_2]$.). (a) General view. (b) Projection along chain direction. 50
Figure 49 Schematic representation of a composite fold surface consisting of adjacently re-entrant folds and various elements of surface looseness. 50
Figure 50 Polymer folding: (a) trans-gauche transitions are low energy modes that help polymers fold well below their persistence length, (b) polyethylene chain fold model used to study the free-energy of the fold surface. The fold conformation shown has six trans-gauche transitions such that the polymer re-enters the crystal in the adjacent lattice site of the lamellae. A diagrammatic representation of chain folding in polymer crystals is shown in (c). 51
Figure 51 Sketch illustrating the tilt due to fold staggering. A single polymer has multiple folds and form ribbons. Left figure shows a ribbon of folded molecule seen normal to the ribbon plane and on the right Stacking of consecutive ribbons seen along the ribbon plane is shown. 51

Figure 52 Schematic representations of polyethylene single crystals: (a) four-sided (lozenge-shaped) tent morphology, (b) six-sided (truncated-lozenge-shaped) tent morphology. The drawing shows the different sectors and its three dimensional shape. The fold direction for a truncated-lozenge in 3D and its top view are shown in (c). The fold directions in each sector is the same as the boundary. 52
Figure 53 The ϕ field which is a solution to Laplace's equation with a point defect sitting at a distance $\vec{\mathbf{r}}_d$ from the center of a circular domain of radius R is shown. 54
Figure 54 Calculated tilt- and hexatic-orientation pattern about the five-armed star defect. The arrows represent the local orientation of the tilt and the crosses the local orientation of the sixfold symmetric bonds (hexatic). 54
Figure 55 Comparison of θ-functions with disclination at the origin: $\theta = \arctan(y/x)$ (left) and $\theta = \arctan\left(\frac{\tanh(y/\omega)}{\tanh(x/\omega)}\right)$ (right, $\omega = 1$). The plateaus corresponding to constant orientation of θ-field can be seen on the right plot. 55
Figure 56 A plot of vector field, $\hat{\mathbf{s}} = \{\cos(\theta), \sin(\theta)\}$, corresponding to eq. 64 is shown in the center plot. Zoomed version of region close to defect core (left) shows a normal disclination like field, but assymptotically far away the solution develops a 1D wall like structure (right). 55
Figure 57 Figure on the left shows the approximate boundary on which the fold order is tangential. On numerical integration of F_{ST} over the region shown, of length L, we get the plot on right. For $L >> \omega$, $F_{ST} \sim L$. 56
Figure 58 Schematic illustrations of different degrees of fineness of slip : (a) fine slip, (b) coarser slip, (c) shearing of a lattice that has a large lattice translation vector in the chain direction. 56

Figure 59 Buckling transition due to inclusion of tilt: (a) A flat lamella with folds but no tilt, (b) constant fold structure with no sectors which on inclusion of tilt will end up in state (c). The cross section of the lamella is shown on top of (c). Fold structure with orthogonal soliton is shown in (d) and (e) is the corresponding buckled tent-structure, along with the tilt structure of the cross-section. 57

Figure 60 Bend structure: both (a) and (b) show cross section of membranes with same curvature. (a) is due to elastic deformation (splay) and (b) is due to plastic deformation (slide). 57

Figure 61 Mean curvature H is concentrated along two straight lines which intersect at right angles. The crystal is split into four sectors with flat regions separated by soliton walls in curvature. (Here $\frac{\tilde{K}}{h_4} = 1$). 63

Figure 62 Plot of height function given by eq.(74) 63

1

INTRODUCTION

Soft matter is a subfield of condensed matter comprising a variety of physical states that are easily deformed by thermal fluctuations. They include liquids, colloids, polymers, foams, gels, granular materials, and a number of biological materials. The key features that are common to all of these materials is that the energy scales of these systems are comparable with the thermal energy. At these temperatures, quantum aspects are generally unimportant.

In this thesis, we study the interplay between shape, order and topological defects in two-dimensional soft condensed matter systems. Curvature and topological defects introduce geometrical frustrations in order. The strength of interactions, type and number of defects, and the ground state that we start with impact the nature of frustration. Different aspects of this problem are addressed in the thesis. The problem on polymer tent morphology (Chapter 4) was the genesis for the all the problems dealt within this thesis.

This chapter presents a short introduction to some notions of soft condensed matter systems that are used in later chapters. Each chapter includes an introduction which motivates and poses the problem.

1.1 SYMMETRY AND ORDER

Soft matter systems show a wide variety of phases which are characterized by their symmetries, i.e. by transformations in orientational and translational ordering in the system. Many soft materials form a disordered (isotropic) phase at high temperatures but adopt ordered structures, with different degrees of translational and orientational order, at low temperatures. The transition from the isotropic phase to ordered phase is said to be a symmetry breaking transition, because the symmetry of the isotropic phase (with full rotational and translational symmetry) is broken at low temperatures.

The thesis deals exclusively with problems that are two dimensional in nature. The physics of 2D condensed matter systems is a rich and mature subject [1]. The field has been rejuvenated by its new found applications to biological systems. Geometry and topology lead to fascinating shapes of membranes and thin films. Everyday experience with soap bubbles, the shape and dazzling structures they take, are deceptive of the hard problems they pose [2]. The mathematics of minimal surfaces, which was motivated by study of soap bubbles, after more than two centuries of work is still rich with open conjectures [3]. A simple model of membrane with curvature elasticity leads to a vast vatiety of non-trivial equilibrium shapes. It has been successful in explaining the disc-like structure of red blood cell [4], shape and fluctuations in lipid bilayers [5], even string like excitations in high energy physics [6].

1.1.1 *Curvature*

A fluid membrane with thickness much smaller than the lateral dimensions can be represented by a two-dimensional mathematical surface. Based on similarities between fluid membranes (lipid bilayers) and nematic liquid crystals, Helfrich [7] proposed the following expression for the curvature energy per unit area

$$f_H = \left(\frac{\kappa}{2} H^2 + \kappa_G K\right) , \tag{1}$$

where H is the mean curvature, K is the Gaussian curvature (or intrinsic curvature), and κ, κ_G are the corresponding elastic constants.

In general for a surface parametrized by (σ_1, σ_2) and represented by position vector $\mathbf{R}(\sigma_1, \sigma_2)$ (see fig. 1), the extrinsic curvature tensor is [6]

$$K_{ij} = \mathbf{t}_i . \partial_j \hat{\mathbf{n}} , \tag{2}$$

where $i, j \in \{1, 2\}$ and $\mathbf{t}_i = \frac{\partial \mathbf{R}}{\partial \sigma^i}$, $\hat{\mathbf{n}} = \frac{\mathbf{t}_1 \times \mathbf{t}_2}{|\mathbf{t}_1 \times \mathbf{t}_2|}$ are the tangents and surface normal respectively. The induced metric is defined by $g_{ij} = \mathbf{t}_i . \mathbf{t}_j$. Then the mean and Gaussian curvatures are related to the curvature tensor by: $H = \frac{1}{2} \mathrm{Tr}(K^i{}_j)$, $K = \mathrm{Det}(K^i{}_j)$.

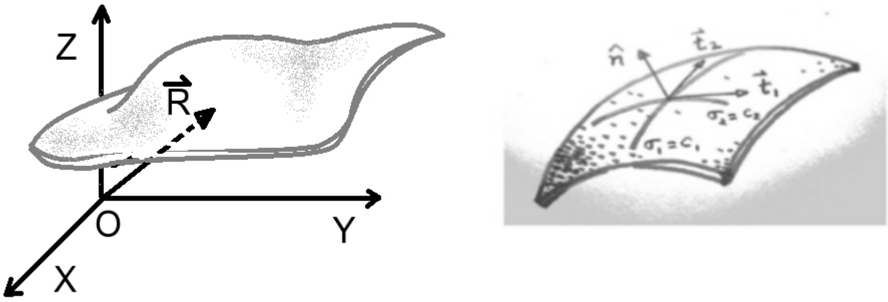

Figure 1: Parametrization of a surface.

1.1.2 *Order*

Introduction of order within the membrane further enriches the shape phase diagram. A 2D membrane can have a vast range of internal orders, with varying degrees of broken symmetries: nematic (director), tilt (vector), hexatic (phase), crystal (strain) to name a few. The terms in the free-energy depend on the symmetry properties of these orders.

1.1.3 *Order + Curvature = Frustration*

In two dimensional systems Gaussian curvature is a source of geometric frustration [8, 9]. In presence of curvature the system may not be able to take up a uniform ordered ground state. As an illustration consider drawing "constant" vector (order) field on the surface of a cube. Fig. 2 captures the essence of geometric frustration. We know the uniform ordered state in a flat plane. When one tries to induce the uniform state onto curved surface by flattening it, the state depends on the "path" of flattening process.

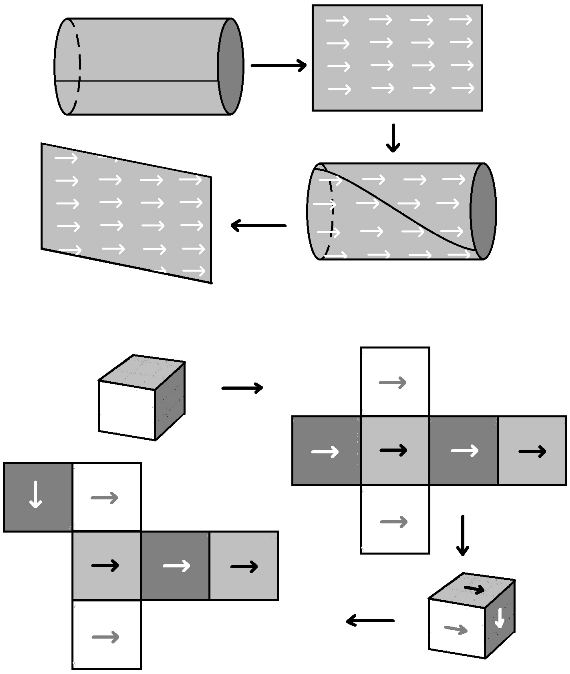

Figure 2: Top: Cylinder is cut open along the axis and flattened to a plane to mark the constant vectors. Now if the cylinder is glued back together and cut in any direction to flatten, the vectors still preserve the directions. Bottom: A cube is opened up and flattened. Constant vectors marked and glued back together. Now if the cube is opened up by cutting along different sets of edges, you find that on flattening vector could change direction. This happens because cube has Gaussian curvature at each corners, where as the cylinder has zero Gaussian curvature.

Note that the frustration is not due to any explicit coupling introduced between order and curvature in the free energy. The frustration is due to the requirement that the order (vector) should be tensorial, i.e. independent of observer ("path").

On the other hand frustrations in order can be screened by curvature. A standard example is tiling a plane by pentagons. On tiling a plane with pentagons gaps open up (see fig. 3), which one can get rid of by stretching the pentagon. But a sphere can be tiled by pentagons, to form dodecahedron, and get a stree-free configuration.

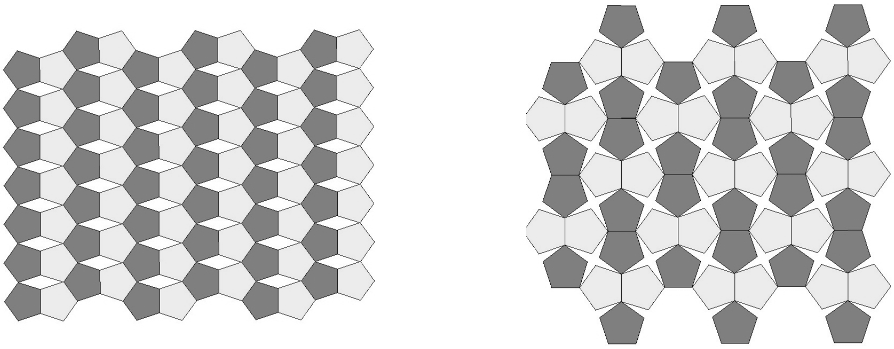

Figure 3: Two different tilings of a plane by pentagons wth gaps.

In chapter 2 we take into account the geometric frustration ("God is in the detail") and derive the equilibrium shape of a membrane with tangent plane order. On the other hand if we force the ordering properties to change through constraints from topology, applied force or introducing defects, the membrane shows tendency to curve/buckle.

1.2 DEFECTS

Topological defects are stable configurations of matter such that small regions of the sample are forced to be discontinuous by the topological behavior of the configuration outside of them. These defects are stable in the sense that they cannot be removed by a purely local perturbation of the material, they must either be moved out to the boundary of the sample or merged into other such topological defects. Based on the symmetry properties of the phase a number of different types of defects are possible.

The type of defect for a system with given symmetry is characterized and classified using homotopy theory [10]. Here an *order parameter space* is defined, which is a space of parameters that describes changes in order parameter[1] that leaves the energy invariant. For example for systems with vector order in 2D, order parameter space is a circle which corresponds to local rotations. Every point on the membrane has an order parameter value, and it depends continuously on the coordinates. Thus a loop on the membrane maps onto a loop in order parameter space. The group structure of loops in the order parameter space can be used to characterize the defects.

In 2D two types of topological point defects are possible, namely disclinations and dislocations (see fig. 4). Disclination is a defect in

---

[1] An order parameter is a measure of the degree of order across the boundaries in a phase transition system; it normally ranges between zero in one phase (usually above the critical point) and nonzero in the other.

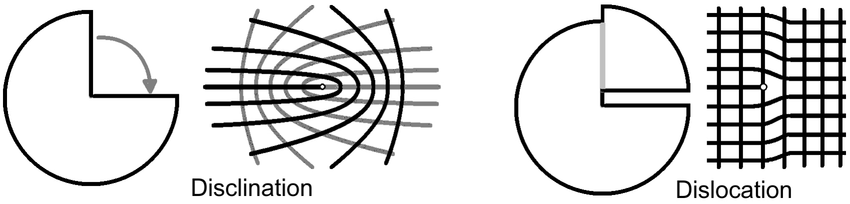

Figure 4: A disclination is obtained by removing or inserting a sector from/into the membrane. In 2D a dislocation can be modeled as a disclination pair (remove and insert back a sector with some translation).

the orientation order whereas a dislocation is a defect in positional order. Just like contour integrals in complex analysis, any contour around the defect (singularity) contains all the information and is the basis for homotopy theory.

The importance of defects in 2D systems were demonstrated from a phase transition point of view by the Berezinsky-Kosterlitz-Thouless transition [11, 12]. Soon after followed by the studies on defect induced melting in 2D crystals [13].

1.2.1 *Order + Defect = Curvature*

Geometric effect of including topological defects are lucidly demonstrated in flexible membranes with crystalline order. Disclinations in crystals are an effect of removal or insertion of sectors of the membrane, and would buckle the membrane into cones [14](see fig. 5, taken from [14]). This notion was used to rationalize the observed icosahedral geometry of virus capsids [15]. Further, studies on dislocations and small angle grain boundaries [16] show how a defective crystal can buckle into a roof like structure (see fig. 6, taken from [16]).

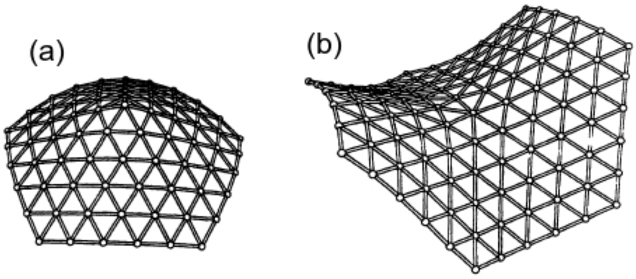

Figure 5: (a) Buckled positive disclination. (b) Buckled negative disclination.

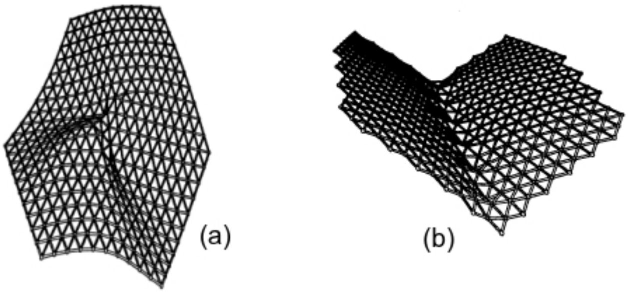

Figure 6: (a) Buckled dislocation pair. (b) Buckled small angle grain boundary, modeled as an array of dislocation pairs.

1.2.2 *Order + Curvature = Defect*

When a membrane with internal order is deposited onto a substrate, the geometry is fixed by the substrate. Then minimal frustration or energy configuration would depend on distribution of defects (density) for the given geometry. Here analogy with electrostatics is used to formulate the problem in terms of Green's function to determine the defect (charge) distribution [17, 18, 19].

1.3 CLASSIFICATION: DEFECT = CURVATURE

In 2D crystals the internal stress or frustration in order due to defects can be completely removed by including Gaussian curvature. Thus crystals with point defects are surfaces with isolated Gaussian curvatures, cone like points, called flat surfaces [20]. In chapter 3 the properties and classification of defects are studied using flat surfaces.

1.4 POLYMER CRYSTAL

One of the long-standing challenges in the field of polymers is to figure out how long interpenetrating and entangled polymer chains organize into crystals upon cooling. Polymer crystals take up a wide range of morphologies based on crystallization conditions [21].

The single crystals of polymers are grown from dilute solutions. Usually such crystals are small, typically a few micrometres across, and are plate-like with a regular shape that reflects that of the crystal unit cell. The thickness is typically 10 nm and take up tent-like structures (see fig. 7, taken from [22]).

The tent structure has similar characteristics as the example systems discussed: roof-like structures, which meet at a cone-like point in the center. From our discussions in previuos sections it seems obvious the crystal has the buckled structure due to presence of defects. But the devil is in the details.

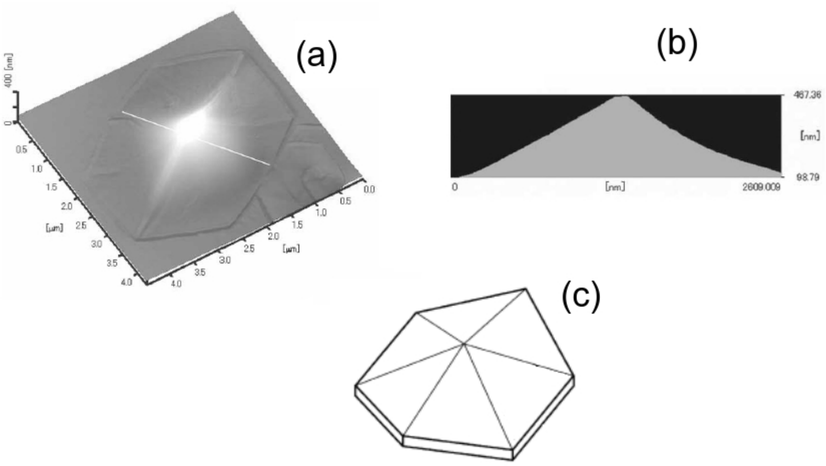

Figure 7: (a) AFM topographic image showing the 3D structure of tent morphology of polyethylene crystal, and (b) is the height field along the line shown in (a). (c) Schematic of the tent structure.

2

EQUILIBRIUM OF FLUID MEMBRANES WITH TANGENT-PLANE ORDER

Fluid membrane can have surprisingly varied structures, the most common example being the cell membrane that is rich in structure as well as functionality.

The radii of curvature involved are small, in other words curvatures are large. For example a human red blood cell is $6-8\mu m$ in diameter, with membrane thickness $\sim 10nm$. Biology is getting quantitative and it appears that it will be increasingly important to solve problems involving the shape and topology of fields by all the technical means (analytical as well as numerics). Moreover we also have to consider free boundary conditions which come up naturally in problems such as translocation of polymer through pores [23].

Very often we cannot obtain analytical solutions to equations of equilibrium and associated boundary conditions, which are non-linear coupled differential equations. But one has to solve them numerically. Nevertheless it always helps to write out the equations in an analytical form, together with the associated free boundary conditions.

The model we are analyzing is the simplest model with vector or nematic order. Also we have not dealt with terms which couple the curvature tensor to the vector [24] or nematic field [19]. It is fairly straight forward to obtain the equations of equilibrium with these higher order couplings included. The free-energy that we are working with is the lowest order that is applicable to both nematic and vector order symmetries. Additional couplings depend on the particular symmetries (nemtaic or vector).

The formulation we choose to analyze directly brings out the connection between shape of the membrane and topology of the field embedded on the membrane. The power of the treatment due to Nelson [9] is particularly significant in pointing out the connection between elasticity and topology.

Our results are summarized in the equations of equilibrium (21), together with boundary conditions (22). As is evident these equations simplify considerably for minimal surfaces ($H = 0$).

2.1 ELASTIC FREE ENERGY OF FLUID MEMBRANES

The Helfrich free energy of a fluid membrane [7] is

$$F_H = \int_M \left(\frac{\kappa}{2} H^2 + \kappa_G K \right) dS, \tag{3}$$

where H is the mean curvature, K is the Gaussian curvature (or intrinsic curvature), and κ, κ_G are the corresponding elastic constants. The integral is over the distorted membrane surface M; $dS = \sqrt{g}\, d\sigma^1\, d\sigma^2$, where $\underline{\sigma} = \{\sigma^1, \sigma^2\}$ parametrizes the surface, and $g = g_{\underline{\sigma}} = \det[g_{\mu\nu}]$ is the determinant of the metric tensor $g_{\mu\nu}$. Gaussian curvature is a total differential [6], integrates to the boundary, and does not contribute to the equations of equilibrium. However, it does contribute to the boundary conditions. Stability conditions demand that κ be positive.

For a membrane with surface tension σ we have the additional contribution

$$F_s = \sigma \int dS, \tag{4}$$

with $\sigma \geqslant 0$ for stability. For a fluid membrane $\sigma = 0$, but one can in principle have tense membrane. So just for the sake of generality we include this term.

F_H and F_s account for the bulk contributions to the elastic free energy. For a membrane with a boundary we also need to consider the contribution from the membrane edge:

$$F_e = \gamma \oint_{\partial M} dl, \tag{5}$$

where γ is the coefficient of line tension. γ has to be positive for stability.

With F_H, F_s and F_e contributing to the total free-energy, Capovilla *et. al* [25] have derived the full equations of equilibrium for a fluid membrane. In what follows we discuss the additional contribution from the tangent plane order.

2.2 ELASTIC FREE ENERGY OF FLUID MEMBRANES WITH TANGENT-PLANE ORDER

2.2.1 *Flat membrane (freeze the bending degree of freedom)*

Nonuniformity in the vector field costs elastic energy. Let $\mathbf{m}(x, y)$ describe the vector order on the flat membrane. The energy density for small deformations in $\mathbf{m}$ has the squared gradient form, it is proportional to $(\partial_i m_j)^2$. The independent invariants [24, 26] allowed by the vectorial symmetry of $\mathbf{m}$ are the squared divergence, and the squared curl of $\mathbf{m}$. To the lowest (harmonic, or linear) order, the free energy for distortions of $\mathbf{m}$ is

$$F_{\mathbf{m}} = \int \left[\frac{K_1}{2} (\nabla \cdot \mathbf{m})^2 + \frac{K_2}{2} (\nabla \times \mathbf{m})^2 \right] dS, \tag{6}$$

where $dS = dx\, dy$. Very often, the “one-constant approximation" $K_1 = K_2 = K_m$ simplifies the problem at hand, and is sufficient to yield qualitative results [26]. Within this approximation (6) reduces to

$$F_{m1} = \frac{K_m}{2} \int (\partial_i m_j)(\partial_i m_j)\, dx\, dy, \tag{7}$$

$\{i,j\} = \{x,y\}$, and we have used the summation convention.

In a general deformation, the magnitude m as well as the orientation θ of the vector field $\mathbf{m} = m\,(\cos\theta, \sin\theta)$ (written in fixed laboratory frame) change. If the magnitude of $\mathbf{m}$ is fixed (or changes in the magnitude are very costly as would be the case deep into the tangent-plane order phase) then $\mathbf{m}$ can be treated as a unit vector $\hat{\mathbf{m}} = (\cos\theta, \sin\theta)$ with simple scaling of coordinates. In this case (7) simplifies further to "low temperature" elasticity [1]

$$F_\theta = \frac{K_m}{2} \int (\nabla\theta)^2\, dx\, dy, \tag{8}$$

where ∇ is the gradient operator in Cartesian coordinates.

2.2.1.1 *Deformable membrane*

On a deformable membrane, the form (7) is still valid, albeit with the replacement of ordinary, Cartesian divergence and curl operators with their covariant versions, and with $dS = \sqrt{g}\, d\sigma^1\, d\sigma^2$.

In the one-constant approximation

$$F_m = \frac{K_m}{2} \int (\nabla_\mu m_\nu)(\nabla^\mu m^\nu)\, dS, \tag{9}$$

where ∇_μ is the covariant partial derivative with respect to σ^μ, $\mu = 1,2$, superscripts (subscripts) denote contravariant (covariant) components, and the summation convention is used.

For deformable membranes the gradient operator has to be modified to account for membrane curvature. Upon traversing a closed loop surrounding a region with curvature, a parallel-transported vector does not return to its original orientation, but comes back rotated [6]. Intrinsic curvature of the membrane necessarily introduces frustration in the $\hat{\mathbf{m}}$- field. To obtain the analogue of the square-gradient elasticity (8) we set up a local, orthonormal frame $\hat{\mathbf{e}}_i(\underline{\sigma})$, $i = \{1,2\}$ in the tangent plane, where $\underline{\sigma} = \sigma^\mu$, $\mu = \{1,2\}$ are internal coordinates on the membrane parametrized via the three-dimensional position vector $\mathbf{R}(\underline{\sigma})$. Thus $\hat{\mathbf{m}}(\underline{\sigma}) = (\cos\theta(\underline{\sigma}), \sin\theta(\underline{\sigma}))$ in the local Cartesian frame. In terms of the tangent vectors $\mathbf{t}_\mu = \partial_\mu \mathbf{R} = \partial\mathbf{R}/\partial\sigma^\mu$, the local Cartesian basis $\hat{\mathbf{e}}_i = E_i{}^\mu\, \mathbf{t}_\mu$, where components of $E_i{}^\mu$ form a 2×2 invertible matrix. $E_i{}^\mu$ is known as the *vierbein* ("four legs" in German) [27]. We reserve Greek letters for the coordinate ($\mathbf{t}$) basis, and Latin letters for the Cartesian ($\hat{\mathbf{e}}$) basis. The $\mathbf{e}$- basis is local, and can have an arbitrary orientation in the tangent plane. Thus there is an $O(2)$-freedom in its choice of the $\hat{\mathbf{e}}$- basis. For deformable membranes the square-gradient elastic free energy [28, 9]

$$F_\theta = \frac{K_A}{2} \int (\boldsymbol{\partial}\theta - \mathbf{A})^2\, dS, \tag{10}$$

where the spin connection $\mathbf{A}$ accounts for membrane curvature. The components $A_\mu = (1/2)\,\epsilon^{ij}\,\hat{\mathbf{e}}_i \cdot \partial_\mu \hat{\mathbf{e}}_j$, where $\epsilon^{12} = -\epsilon^{21} = 1$, $\epsilon^{11} = \epsilon^{22} = 0$ is the antisymmetric symbol. In (10),

$$(\boldsymbol{\partial}\theta - \mathbf{A})^2 = (\partial_\mu\theta - A_\mu) g^{\mu\nu} (\partial_\nu\theta - A_\nu),$$

the area element $dS = \sqrt{g}\, d\sigma^1\, d\sigma^2$, g is the determinant of the metric $g_{\mu\nu} = \mathbf{t}_\mu \cdot \mathbf{t}_\nu$, and $g^{\mu\nu}$ is the inverse of $g_{\mu\nu}$. The free energy (10) is invariant under the local gauge transformation $\theta \to \theta + \psi$, $\mathbf{A} \to \mathbf{A} + \boldsymbol{\partial}\psi$.

The geometry of the membrane and the topology of the θ- field are connected via [17]

$$\nabla \times \boldsymbol{\partial}\theta = s\,\hat{\mathbf{n}}, \tag{11}$$

$$\nabla \times \mathbf{A} = K\,\hat{\mathbf{n}}, \tag{12}$$

where $\hat{\mathbf{n}}$ is the unit normal to the membrane,

$$s(\underline{\sigma}) = 2\pi \sum_m q_m\, \delta(\underline{\sigma} - \underline{\sigma}_m)/\sqrt{g} \tag{13}$$

is density of disclination charges q_m located at $\underline{\sigma}_m$ [17], and $K(\underline{\sigma})$ is the Gaussian curvature.

In what follows we first discuss the (Euler-Lagrange) equation of equilibrium for F_θ corresponding to variations in the θ- field, keeping the shape of the membrane fixed. It is straightforward to obtain the θ- equation [17]

$$\frac{\delta F_\theta}{\delta\theta} = \nabla \cdot \mathcal{D}\theta = 0, \tag{14}$$

where we have introduced the notation $\mathcal{D}\theta = (\boldsymbol{\partial}\theta - \mathbf{A})$, and the covariant divergence of a vector field $\mathbf{V}$ is given by

$$\nabla \cdot \mathbf{V} = (1/\sqrt{g})\, \partial_\mu (\sqrt{g}\, V^\mu)$$

. The variational problem of minimizing F_θ also gives the free boundary condition. On the boundary $\mathbf{R}_{(b)}(s)$ of the membrane parametrized in terms of the arc-length s,

$$\hat{\mathbf{n}}_{(b)} \cdot \partial\theta = 0, \tag{15}$$

where the unit outward normal to the membrane boundary $\hat{\mathbf{n}}_{(b)} = \hat{\mathbf{t}}_{(b)} \times \hat{\mathbf{n}}$, with unit tangent to the boundary $\hat{\mathbf{t}}_{(b)} = \partial \mathbf{R}_{(b)}(s)/\partial s$, and unit normal to the membrane $\hat{\mathbf{n}}$ (see fig. 8).

Next, we vary the shape $\mathbf{R}(\underline{\sigma})$ of the membrane, keeping the θ- field fixed. For the shape variation we set

$$\delta\mathbf{R} = \mathbf{t}_\mu\, \delta R^\mu_{\|} + \hat{\mathbf{n}}\, \delta R_\perp, \tag{16}$$

where $\delta\mathbf{R}_{\|}$ and $\delta R_\perp$ are, respectively, the variations in the tangent plane of the membrane and along its normal. Only the normal variations $\delta R_\perp$ contribute to the bulk equations of shape equilibrium

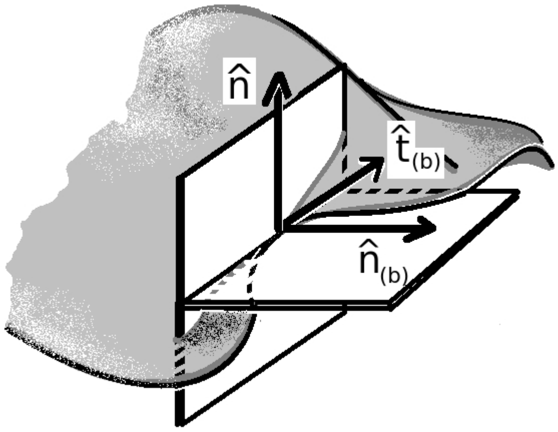

Figure 8: Darboux frame $\left\{\hat{\mathbf{t}}_{(b)}, \hat{\mathbf{n}}, \hat{\mathbf{n}}_{(b)}\right\}$ for a membrane with boundary.

(the Euler-Lagrange equations), whereas variations along the tangent plane $\delta R_{\|}^{\mu}$ (diffiomorphisms) contribute to the boundary conditions [25]. In carrying out the shape variation, we wish to keep the θ- field fixed ($\delta\theta = 0$). A covariant (coordinate-independent) way of accomplishing this [29] is shown in fig. 9. In the figure the white curves labelled Σ and Σ' represent integral curves (field- lines) of the $\hat{\mathbf{m}}$- field on the undeformed ($\mathcal{M}$) and deformed ($\mathcal{M}'$) membrane respectively. The $\hat{\mathbf{m}}$-field connects two nearby points $\mathbf{R}(\underline{\sigma})$ and $\mathbf{R}(\underline{\sigma} + d\underline{\sigma})$ on Σ. Upon shape variation along the membrane normal, $\mathbf{R}'(\underline{\sigma}) = \mathbf{R}(\underline{\sigma}) + \hat{\mathbf{n}}(\underline{\sigma})\ \delta R_{\perp}(\underline{\sigma})$, and $\mathbf{R}'(\underline{\sigma} + d\underline{\sigma}) = \mathbf{R}(\underline{\sigma} + d\underline{\sigma}) + \hat{\mathbf{n}}(\underline{\sigma} + d\underline{\sigma})\ \delta R_{\perp}(\underline{\sigma} + d\underline{\sigma})$ on Σ. The Lie-dragged vector $\hat{\mathbf{m}}$ then connects the points $\mathbf{R}'(\underline{\sigma})$ and $\mathbf{R}'(\underline{\sigma} + d\underline{\sigma})$.

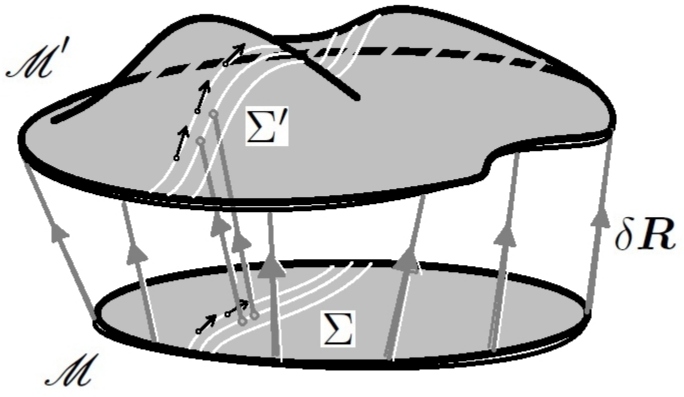

Figure 9: Lie dragging the $\hat{m}$ - field.

We begin by finding the variation of the spin connection $A_\mu = (1/2)\,\epsilon^{ij}\,\hat{\mathbf{e}}_i \cdot \partial_\mu \hat{\mathbf{e}}_j$, with $\hat{\mathbf{e}}_k = E_k{}^{\mu}\mathbf{t}_\mu$. In the $\mathbf{t}$- basis

$$\delta\mathbf{e}_k = (\delta E_k{}^{\mu} + E_k{}^{\nu}\delta U_\nu{}^{\mu})\,\mathbf{t}_\mu + E_k{}^{\mu}\delta V_\mu\,\hat{\mathbf{n}}, \tag{17}$$

where we used $\delta \mathbf{t}_\mu = \delta U_\nu{}^\mu\, \mathbf{t}_\mu + \delta V_\mu\, \hat{\mathbf{n}}$ with $\delta U_\nu{}^\mu = \nabla_\nu \delta R^\mu_\parallel + K_\nu{}^\mu$, $\delta V_\mu = \nabla_\mu \delta R_\perp + K_{\mu\nu} \delta R^\mu_\parallel$, with ∇ representing the covariant gradient operator, and $K_{\mu\nu}$ the curvature tensor. In the $\hat{\mathbf{e}}$- basis

$$\delta \mathbf{e}_k = \epsilon_k{}^l \hat{\mathbf{e}}_l\, \delta_\parallel + \hat{\mathbf{n}}\, \delta_\perp, \tag{18}$$

where $\delta_{\parallel,\perp} = \delta_{\parallel,\perp}(\underline{\sigma})$ are small variations. The term involving $\delta_\parallel$ corresponds to (infinitesimal) rigid anticlockwise rotation of the $\hat{\mathbf{e}}$-basis, and reflects the local gauge freedom. We fix the gauge by setting $\delta_\parallel = 0$ (this is most simply done by setting $\hat{\mathbf{e}}_1$ parallel to $\mathbf{t}_1$). A comparison of (17) and (18) then gives $\delta E_k{}^\mu = -E_k{}^\nu \delta U_\nu{}^\mu$, and $\delta \mathbf{e}_k = E_k{}^\mu \delta V_\mu \hat{\mathbf{n}}$. Substituting for $\delta \mathbf{e}_k$ in $\delta A_\mu = (1/2)\, \epsilon^{ij}\, \delta(\hat{\mathbf{e}}_i \cdot \partial_\mu \hat{\mathbf{e}}_j)$ gives $\delta A_\mu = \epsilon^{ij} E_i{}^\alpha \delta V_\alpha E_j{}^\sigma K_{\sigma\mu}$. Using $E_i{}^\alpha E_i{}^\sigma = g^{\alpha\sigma}$ and the properties of the antisymmetric symbol it can be shown that $\epsilon^{ij} E_i{}^\alpha E_j{}^\sigma = \epsilon^{\alpha\sigma}/\sqrt{g} = \gamma^{\alpha\sigma}$ (see appendix A.2), the unit covariant antisymmetric tensor. Thus

$$\delta A_\mu = \gamma^{\alpha\sigma} K_{\sigma\mu}\, (\nabla_\alpha\, \delta R_\perp + K_{\alpha\gamma}\, \delta R^\gamma_\parallel). \tag{19}$$

Although $\mathbf{A}$ does not transform as a vector (just as the Christoffel connection, $\Gamma^i{}_{jk}$ does not transform as a tensor), $\delta \mathbf{A}$ does transform like one, as evidenced by (19). Using (19), we obtain

$$\frac{\delta F_\theta}{\delta R_\perp} = K_A \left[\gamma^{\alpha\beta} K_\beta{}^\mu \nabla_\alpha \mathcal{D}_\mu \theta - K^{\mu\nu} (\mathcal{D}_\mu \theta)(\mathcal{D}_\nu \theta) - H (\mathcal{D}\theta)^2 \right] \tag{20}$$

for the first variational derivative of the elastic free energy (10) with respect to shape changes. In writing (20) we have discarded the term $K_A\, (\mathcal{D}_\mu \theta)\, \gamma^{\alpha\beta} \nabla_\alpha K_\beta{}^\mu$ obtained through the variation, assuming single-valued parametrization of membrane patches; $\gamma^{\alpha\beta} \nabla_\alpha K_\beta{}^\mu = 0$. The second and third terms on the right hand side of (20) result from the normal variations of the $g_{\mu\nu}$ and $\sqrt{g}$ factors in the elastic free energy (10) respectively.

Together with the known normal variations of the bend energy and the surface tension terms (as given in for example in [25]) we have the Euler-Lagrange equation for normal variation (also called the shape equation)

$$\frac{\delta F_\theta}{\delta R_\perp} + \frac{\kappa}{2} \left[2H(H^2 - K) + \nabla^2 H \right] - 2\sigma H = 0, \tag{21}$$

for a membrane free of body forces. In (21) above, the first term is given by (20).

The variational problem of minimizing the total elastic free energy (10) also yields free boundary conditions for membranes with a boundary (edge). This is most conveniently done by describing the bounding curve in the arc-length parametrization $\mathbf{R}(s)$, and employing a Darboux frame comprising of the unit tangent to the boundary $\hat{\mathbf{t}}_{(b)}(s) = \partial \mathbf{R}(s)/\partial s$, the unit surface normal at the boundary $\hat{\mathbf{n}}(s)$, and the unit outward normal to the boundary $\hat{\mathbf{n}}_{(b)}(s) = \hat{\mathbf{t}}_{(b)}(s) \times \hat{\mathbf{n}}(s)$. We use the notation $\nabla_{\|} = t^{\mu}_{(b)}\nabla_{\mu}$, $\nabla_{\perp} = n^{\mu}_{(b)}\nabla_{\mu}$, $K_{\|} = t^{\mu}_{(b)}t^{\nu}_{(b)}K_{\mu\nu}$, $K_{\perp} = n^{\mu}_{(b)}n^{\nu}_{(b)}K_{\mu\nu}$, $K_{\|\perp} = t^{\mu}_{(b)}n^{\nu}_{(b)}K_{\mu\nu}$, $\mathcal{D}_{\|} = t^{\mu}_{(b)}\mathcal{D}_{\mu}$, and $\mathcal{D}_{\perp} = n^{\mu}_{(b)}\mathcal{D}_{\mu}$. Corresponding respectively to variations along $\hat{\mathbf{n}}_{(b)}$, $\hat{\mathbf{n}}$, and $\hat{\mathbf{t}}_{(b)}$, we have the following free boundary conditions accompanying the shape equation:

$$\frac{K_A}{2}\left[(\mathcal{D}\theta)^2 + (\mathcal{D}_{\perp}\theta)^2\right] + \frac{\kappa}{2}H^2 + \kappa_G K + \gamma k_g + \sigma = 0, \tag{22}$$

$$K_A\,(\mathcal{D}_{\|}\theta)K_{\|} - \kappa\nabla_{\perp}H + \kappa_G\nabla_{\|}K_{\|\perp} - \gamma K_{\|} = 0, \tag{23}$$

$$\kappa H + \kappa_G K_{\|} = 0. \tag{24}$$

2.3 COULOMB GAS MODEL

As pointed out in [17], it is convenient to define the Airy stress function χ via $\mathcal{D}^{\mu}\theta = \gamma^{\mu\nu}\partial_{\nu}\chi$ so that the θ- equation (14) is identically satisfied. However, χ has to obey the condition [17]

$$\nabla^2\chi = s - K \tag{25}$$

that ensures compatibility between the shape of the membrane and topology of the vector field embedded in it. To the lowest order, the shape variation (21), that we have derived reduces to the “nonlinear, hexatic von Kármán equation"

$$\frac{\kappa}{K_A}\nabla^4 f = (\partial_y^2\chi)(\partial_x^2 f) + (\partial_x^2\chi)(\partial_y^2 f) - 2(\partial_x\partial_y\chi)(\partial_x\partial_y f), \tag{26}$$

obtained by Deem and Nelson [17] using the Monge gauge height function $f(x,y)$. The free boundary conditions can also easily be recast in terms of χ.

The formulation as developed above is amenable to be recast in terms of the "source theory" of Schwinger [30]. Using Airy stress function (10) can be rewritten as,

$$F_{\theta} = \frac{K_A}{2}\int_{\mathcal{M}} (\nabla\chi)^2\,\sqrt{g}\,d^2\sigma\,. \tag{27}$$

The final free energy can be written in terms of source function $\rho(\underline{\sigma})$ as [17]

$$F_{\theta} = \frac{K_A}{2}\int\!\!\int \rho(\underline{\sigma})\;G(\underline{\sigma},\underline{\sigma}')\;\rho(\underline{\sigma}')\;dS\;dS'\,, \tag{28}$$

where the Green’s function $G\left(\underline{\sigma},\underline{\sigma}'\right)$ is defined via

$$\nabla^2_{\underline{\sigma}}G\left(\underline{\sigma},\underline{\sigma}')\right) = \frac{\delta^{(2)}\left(\boldsymbol{R}(\underline{\sigma}) - \boldsymbol{R}(\underline{\sigma}')\right)}{\sqrt{g(\underline{\sigma})}}\,. \tag{29}$$

Normal variation of (29) gives,

$$\nabla^2\delta_{\perp}G = -\nabla_{\mu}\delta V^{\mu}\,, \tag{30}$$

where $\delta V^{\mu} = (H\, g^{\mu\nu} - 2K^{\mu\nu})\, \delta R_{\perp} \nabla_{\nu} G$. The equlibrium shape of a membrane with tangent plane order were derived in [31] implicitly assuming the Green's function to be invariant with respect to shape variation, but (30) above clearly shows this is not true. Further, we have verified that variation in F_{θ} using (30) gives back the results (21) derived in the previous section.

This formulation which is traditionally used in the context of membranes can also to applied to liquid crystals such as Sm-C, Sm-C* etc. We are in the process of applying this formalism to consider dispirations in Sm-C* [32, 33].

Appendices

A

DIFFERENTIAL GEOMETRY

A.1 DERIVATION OF THE COVARIANT VERSION IN TERMS OF θ

The new, local, Euclidean basis vectors can always be written as a linear combination of the tangent vectors in the coordinate basis:

$$\hat{\mathbf{e}}_i = E_i{}^{\mu}\, \mathbf{t}_{\mu}, \tag{31}$$

where $\hat{\mathbf{e}}_i$, $i = 1, 2$, forms the new, orthonormal basis, $\mathbf{t}_{\mu} = \partial \mathbf{R} / \partial \sigma^{\mu}$, $\mu = 1, 2$, are the tangent vectors in the old coordinates $\underline{\sigma}$, and the components of $E_i{}^{\mu}$ form a 2×2 invertible matrix. Following standard notation, we reserve Greek letters for the coordinate basis, and Latin letters for the orthonormal basis. In terms of the local orthonormal basis $\hat{\mathbf{e}}_i$, the coordinate basis $\mathbf{t}_{\mu}$ can therefore be written by switching the indices on the vielbein,

$$\mathbf{t}_{\mu} = E_{\mu}{}^{i}\, \hat{\mathbf{e}}_i, \tag{32}$$

where

$$\begin{aligned} E_i{}^{\mu} E_{\mu}{}^{j} &= \delta_i^j, \\ E_{\mu}{}^{i} E_i{}^{\nu} &= \delta_{\mu}^{\nu}, \end{aligned} \tag{33}$$

where δ_{μ}^{ν}, δ_i^j are Kronecker deltas. Since the new basis $\hat{\mathbf{e}}_i$ is orthonormal,

$$g_{\mu\nu}\, e^{\mu}{}_{i}\, e^{\nu}{}_{j} = \eta_{ij}, \tag{34}$$

where $g_{\mu\nu} = \mathbf{t}_{\mu} \cdot \mathbf{t}_{\nu}$ is the coordinate metric and is the η_{ij} is the Euclidean (flat) metric. The coordinate metric

$$g_{\mu\nu} = e_{\mu}{}^{i}\, e_{\nu}{}^{j}\, \eta_{ij}. \tag{35}$$

Using the orthonormal basis and the vielbein, any vector $\mathbf{V} = V^{\mu} \mathbf{t}_{\mu}$ in the tangent plane of the membrane can be written as $\mathbf{V} = V^{i}\, \hat{\mathbf{e}}_i$, with $V^{i} = E^{i}{}_{\mu} V^{\mu}$. In the Euclidean basis, we can now express any vector in the required form $\mathbf{V} = V(\cos\theta, \sin\theta)$, where V is the magnitude of $\mathbf{V}$. The two metrics can be used to raise and lower the indices on vielbeins, for example $E_{\mu i} = g_{\mu\nu} E^{\nu}{}_{i}$. Vielbeins facilitate conversion of tensors into the Euclidean basis and *vice versa*. The local orthonormal frame can have an arbitrary orientation in the tangent plane. *It is important to note that there is an* $O(2)$*- freedom in choosing the local, orthonormal basis at a point on the membrane.*

Having defined θ, we now define covariant derivatives of a vector field $V_i(\underline{\sigma})$ written in the orthonormal basis. In the *coordinate basis* the covariant derivative

$$\nabla_\mu V^\nu = \partial_\mu V^\nu + \Gamma^\nu{}_{\mu\lambda} V^\lambda, \tag{36}$$

where the term with the Christoffel connection $\Gamma^\nu{}_{\mu\lambda}$ accounts for the change in $\mathbf{V}(\underline{\sigma})$ under parallel transport through $d\sigma^\mu$ on the curved surface [6]. In analogy, let us write

$$\nabla_\mu V^i = \partial_\mu V^i + \omega_\mu{}^i{}_j V^j, \tag{37}$$

and investigate the new connection $\omega_\mu{}^i{}_j$ that, like the vielbein, has mixed indices.

The strategy for expressing the new connection in terms of the Christoffel connection is to compare the expression for the covariant differential of a vector (a tensor, and therefore a coordinate independent object) in the coordinate basis to that written in a mixed basis (using vielbeins). The covariant differential in the coordinate basis

$$\begin{aligned} \nabla \mathbf{V} &= (\nabla_\mu V^\nu)\, d\sigma^\mu \otimes \mathbf{t}_\nu \\ &= (\partial_\mu V^\nu + \Gamma^\nu{}_{\mu\lambda} V^\lambda)\, d\sigma^\mu \otimes \mathbf{t}_\nu. \end{aligned} \tag{38}$$

In the local, orthonormal basis

$$\begin{aligned} \nabla \mathbf{V} &= (\nabla_\mu V^i)\, d\sigma^\mu \otimes \mathbf{t}_i \\ &= (\partial_\mu V^i + \omega_\mu{}^i{}_j V^j)\, d\sigma^\mu \otimes \mathbf{t}_i \\ &= \{\partial_\mu (E^i{}_\nu V^\nu) + \omega_\mu{}^i{}_j E^j{}_\lambda V^\lambda\} d\sigma^\mu\, E_i{}^\sigma \otimes \mathbf{t}_\sigma \\ &= E^\sigma{}_i (E^i{}_\nu \partial_\mu V^\nu + V^\nu \partial_\mu E_\nu{}^i + \omega_\mu{}^i{}_j E^j{}_\lambda V^\lambda)\, d\sigma^\mu \otimes \mathbf{t}_\sigma \\ &= \{\partial_\mu V^\nu + E^\nu{}_i (\partial_\mu E^i{}_\lambda) V^\lambda + E^\nu{}_i \omega_\mu{}^i{}_j E^j{}_\lambda V^\lambda\} d\sigma^\mu \otimes \mathbf{t}_\nu. \end{aligned} \tag{39}$$

Thus

$$\Gamma^\nu{}_{\mu\lambda} = E^\nu{}_i (\partial_\mu E^i{}_\lambda) V^\lambda + E^\nu{}_i \omega_\mu{}^i{}_j E^j{}_\lambda V^\lambda, \tag{40}$$

or,

$$\omega_\mu{}^i{}_j = E^i{}_\nu \Gamma^\nu{}_{\mu\lambda} E^\lambda{}_j - E_j{}^\lambda \partial_\mu E_\lambda{}^i. \tag{41}$$

The new connection in the mixed basis $\omega_\mu{}^i{}_j$ called the *spin connection* because it is used to define the covariant derivatives of spinor fields in curved space-time [28]. The spin connection is not a tensor. *Note that the placement of the Latin indices (up or down) is not important since these refer to a local, orthonormal basis.*

The relation (41) can be used to show that the covariant derivative of the vielbein vanishes. First, we note that the covariant derivative of a mixed, second rank tensor written in the mixed (part- old, part-new) basis

$$\nabla_\mu T_\sigma{}^i = \partial_\mu T_\sigma{}^i - \Gamma_{\mu\sigma}{}^\nu T_\nu{}^i + \omega_\mu{}^i{}_j T^j{}_\sigma, \tag{42}$$

where we have used the Christoffel connection as well as the spin connection. Next, we multiply the expression for the spin connection in terms of the Christoffel connection (41) by $E^j{}_\sigma$ to write

$$\omega_\mu{}^i{}_j E^j{}_\sigma = E^i{}_\nu \Gamma^\nu{}_{\mu\sigma} - \partial_\mu E^i{}_\sigma. \tag{43}$$

A comparison of (42) and (43) above shows that

$$\nabla_\mu E^i{}_\sigma = 0, \tag{44}$$

a result that is known as the "tetrad postulate".

We now show that the spin connection is antisymmetric in its Latin indices, using the fact that the covariant derivative of the metric vanishes (*i.e.*, the metric is compatible).

$$\begin{aligned}\nabla_\mu \eta_{ij} &= \partial_\mu \eta_{ij} - \omega_\mu{}^k{}_i \eta_{kj} - \omega_\mu{}^k{}_j \eta_{ki} \\ &= -\omega_{\mu ij} - \omega_{\mu ji} \\ &= 0,\end{aligned} \tag{45}$$

implying $\omega_{\mu ij} = -\omega_{\mu ji}$. This antisymmetry allows us to write

$$\omega_{\mu ij} = \epsilon_{ij} A_\mu, \tag{46}$$

thus introducing the vector field $\mathbf{A}$ (in two dimensions $\omega_{\mu ij}$ has only two independent components, given that it is antisymmetric in the Latin indices). We now derive an explicit formula for $\mathbf{A}$, using the expression (41) for the spin connection in terms of the Christoffel connection. Notice that the Christoffel connection

$$\Gamma_{\mu\lambda}{}^\nu = \mathbf{t}^\nu \cdot \partial_\mu \mathbf{t}_\lambda, \tag{47}$$

where we have used $\nabla_\mu \mathbf{t}_\lambda = K_{\mu\lambda}\,\hat{\mathbf{n}} = \partial_\mu \mathbf{t}_\lambda - \Gamma_{\mu\lambda}{}^\sigma \mathbf{t}_\sigma$. Using the properties of vielbeins and substituting for $\Gamma_{\mu\lambda}{}^\nu$ in (41),

$$\begin{aligned}\omega_\mu{}^i{}_j &= E_j{}^\lambda \left(\hat{\mathbf{e}}_i \cdot \partial_\mu \mathbf{t}_\lambda - \partial_\mu E_\lambda{}^i\right) \\ &= \hat{\mathbf{e}}^i \cdot \left[\partial_\mu (E_j{}^\lambda \mathbf{t}_\lambda) - \mathbf{t}_\lambda\, \partial_\mu E^\lambda{}_j\right] - E_j{}^\lambda \partial_\mu E_\lambda{}^i \\ &= \hat{\mathbf{e}}^i \cdot \partial_\mu \hat{\mathbf{e}}_j - E^i{}_\lambda \partial_\mu E^\lambda{}_j - E_j{}^\lambda \partial_\mu E_\lambda{}^i \\ &= \hat{\mathbf{e}}^i \cdot \partial_\mu \hat{\mathbf{e}}_j,\end{aligned} \tag{48}$$

i.e.,

$$A_\mu = \frac{1}{2}\epsilon^{ij}\,\hat{\mathbf{e}}_i \cdot \partial_\mu \hat{\mathbf{e}}_j, \tag{49}$$

where ϵ_{ij} is the antisymmetric (Levi-Civita) symbol.

The spin connection involves derivatives of the local orthonormal basis vectors, and tells us how the local orthonormal basis changes its orientation along coordinate tangent vectors. As we have seen the curvature tensor is the projection of the the derivatives of the coordinate tangent vectors onto the surface normal. We therefore expect that the spin connection and the curvature tensor to be related. The form of covariant derivatives defined using Christoffel connection and spin connection is identical, moreover, the Riemann curvature can be written solely in terms of the Christoffel connection and its derivatives. This buttresses our expectation. In fact, show below that the curl of **A** is the Gaussian curvature (this result is true for two-dimensional surfaces embedded in three-dimensional Euclidean space).

To do this, it is convenient to write the Riemann curvature tensor in the mixed basis. Using vielbeins, and the symmetry $R_{\alpha\beta\mu\nu} = R_{\mu\nu\alpha\beta}$, we have

$$\begin{aligned} R_{\mu\nu ij} &= R_{\mu\nu\alpha\beta}\, E^{\alpha}{}_{i}\, E^{\beta}{}_{j} = E_{i}{}^{\alpha}\, E_{j}{}^{\beta}\, R_{\alpha\beta\mu\nu} = E_{i}{}^{\alpha} g_{\alpha\lambda}\, E_{j}{}^{\beta} g_{\beta}{}^{\sigma}\, R^{\lambda}{}_{\sigma\mu\nu} \\ &= E_{j}{}^{\sigma} E_{i\lambda} \left(\partial_{\mu}\Gamma^{\lambda}{}_{\sigma\nu} - \partial_{\nu}\Gamma^{\lambda}{}_{\mu\sigma} + \Gamma^{\lambda}{}_{\mu\alpha}\Gamma^{\alpha}{}_{\nu\sigma} + \Gamma^{\lambda}{}_{\nu\alpha}\Gamma^{\alpha}{}_{\mu\sigma}\right), \end{aligned} \tag{50}$$

where we have written the Riemann curvature tensor in terms of the Christoffel connection in the last step. We now claim that the *spin curvature* [34]

$$S_{\mu\nu ij} = \partial_{\mu}\Omega_{\nu ij} - \partial_{\nu}\Omega_{\mu ij} + \Omega_{\mu ik}\Omega_{\nu}{}^{k}{}_{j} + \Omega_{\nu ik}\Omega_{\mu}{}^{k}{}_{j}, \tag{51}$$

obtained by crassly “replacing" Christoffel connections in (50) by spin connections is identically equal to $R_{\mu\nu ij}$. Proving the claim is straightforward but tedious. We do not give the details of the calculation, except pointing out that it is based upon the identity (41) relating spin connection to Christoffel connection, judicious insertion of vielbeins, and their properties (32) - (35) [34].

A.2 ANTI-SYMMETRIC TENSOR

The term $\epsilon^{ij}E_{i}{}^{\alpha}E_{j}{}^{\beta}$ is anti-symmetric in α, β, and

$$\left(\epsilon^{ij}E_{i}{}^{\alpha}E_{j}{}^{\beta}\right)\left(\epsilon^{lk}E_{k}{}^{\mu}E_{l}{}^{\nu}\right) = \left(g^{\alpha\mu}g^{\beta\nu} - g^{\alpha\nu}g^{\beta\mu}\right) . \tag{52}$$

Thus $\epsilon^{ij}E_{i}{}^{\alpha}E_{j}{}^{\beta} = \frac{\epsilon^{\alpha\beta}}{\sqrt{g}} = \gamma^{\alpha\beta}$ (Levi-Civita tensor [6]).

3

CLASSIFICATION OF 2D CRYSTAL GROUND STATES

A carbon nanotube can be made by rolling graphene sheets into cylinders of ~ 1 nanometer diameter. Due to hexagonal symmetry of graphene one can choose a range of rolling directions (see fig. 10, taken from [35]) w.r.t basis vectors of the lattice. Experimental [36] and theoretical [37] analysis show that the mechanical and electronic properties change drastically with the rolling direction. Thus there is a need to characterize the different structural properties of the tube. If $\{\vec{a},\vec{b}\}$ are the basis vectors of the hexagonal lattice, then two integers, $[m,n]$, corresponding to rolling vector $(m\,\vec{a}+n\,\vec{b})$ uniquely specifies the curvature and rolling direction of a tube.

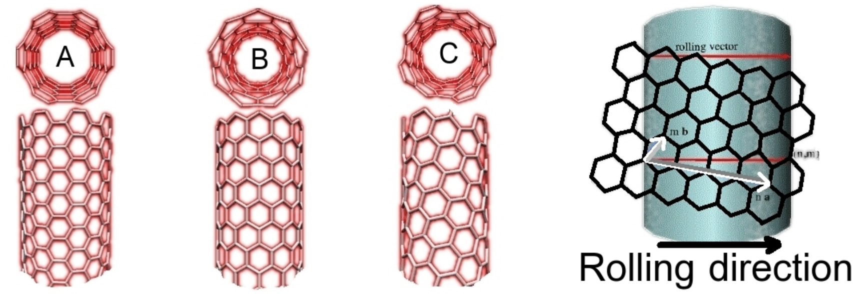

Figure 10: Based on the rolling direction of graphene, the nano tubes are classified as, A: Arm chair, B: Zig-Zag, C: Chiral.

In addition to tubular structures carbon nanotori have been observed experimentally [38] and show high paramagnetic moments. This paramagnetic moment has been shown to depend critically on the crystalline structure [39]. Here along with rolling vector one has to additionally specify the length of the tube used to form the torus. Also, electronic properties of fullerenes with higher genus have been studied numerically [40] (see fig. 11, taken from [40]).

To study elastic properties of above mentioned systems one needs to specify the ground/reference state. In linear elasticity, where the strain $u_{ij} = (g_{ij} - \bar{g}_{ij})$, the difference between the metrics corresponding to deformed body and that of the undeformed (reference) state of the body, usually the reference state $\bar{g}_{ij} = \delta_{ij}$, the Kronecker delta. On a manifold, even though the metrics coincide locally at each patch, globally they may differ. Consider the case of a torus. Torus admits flat, everywhere constant metric in 4d [41] (see fig.12). But it still can have structures which cannot be deformed to each other smoothly (fig. 13).

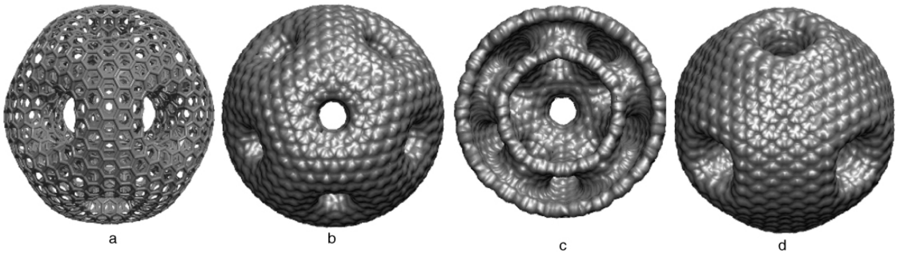

Figure 11: High genus fullerenes with heptagons and hexagons (no pentagons) holey balls. (a) Two-fold axis of a 2040-atom genus 11 fullerene. (b) Five-fold axis. (c) Cut perpendicular to the five-fold axis. (d) A genus 5 holey ball with 1896 atoms.

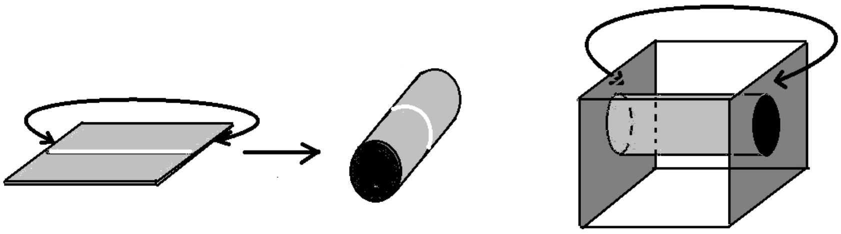

Figure 12: A circle can be made straight (geodesic), such that its curvature w.r.t. the surface it is sitting in (geodesic curvature) is zero, by embedding the circle on a cylinder as shown in the left. Similarly a flat (zero Gaussian curvature) torus can be obtained by embedding a flat cylinder in a 3d box, such that the open ends of the cylinder lie on opposite faces of the box as shown in the right figure. And then the opposite faces of the box are identified without stretching in 4d. On identification of the opposite faces, the cylinder becomes a torus. Notice that as in the case of the circle, the torus is flat w.r.t. the box.

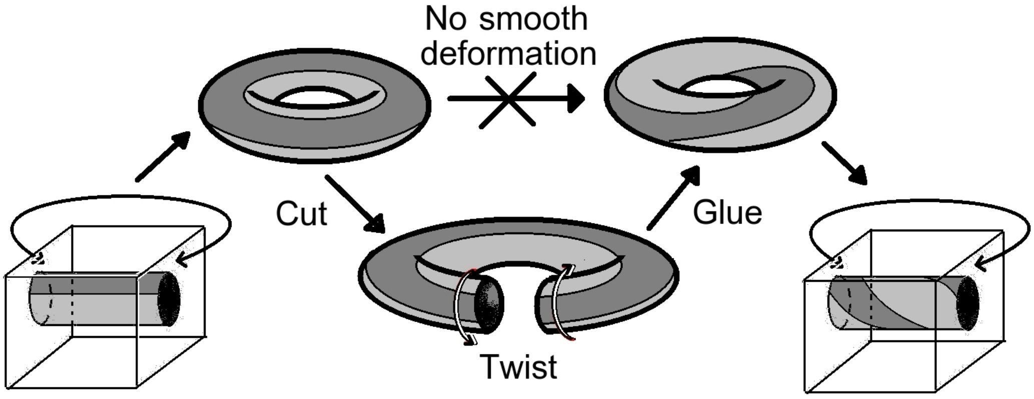

Figure 13: Chocolate-glazed doughnuts: Two different covers of a torus, of the same geometry that are not deformable into each other, which are not deformable to each other. With the loop formed by the boundary of chocolate representing a coordinate axis, the two tori have different winding numbers.

This shows that although $\bar{g}_{ij}$ is Cartesian in each patch, its global structure (like winding number) is left unspecified. To proceed with linear theory of elasticity, this structure has to be fixed. So what are the different $\bar{g}_{ij}$'s possible? how many are there and how to parametrize them? These are the questions of interest. In this chapter we classify the different possible reference metrics, $\bar{g}_{ij}$, in the sense made clear in sec. 3.3.2.

The case of torus with different possible metrics has been widely studied in mathematics literature from different points of view (Alebraic geometry [42], complex analysis [43], differential topology [44], number theory [45]). Although its relevence to study of crystals has been pointed out [34, 46, 47], no serious analysis exists in literature.

Further the crystal can have topological defects such as disclinations and dislocations (see fig. 15). Presence of defects in crystal leads to internal stresses. A collection of defects are modeled in the continuum as defect density field. A 2d crystal can relax its stress by buckling into the 3rd dimension. The buckled shape of a 2d crystal in presence of a single disclination was studied in [14]. Their asymptotic analysis shows that for a strain-free case (i.e. $g_{ij} = \bar{g}_{ij}$) the shape tends towards a cone, with the defect sitting at the apex. At the nanoscale level, when virus capsids are modeled as made up of 2d elastic sheets [48], they have a facetted surface, with disclinations sitting at cone like regions. Hence contrary to the realization of $\bar{g}_{ij}$ as a smooth differentiable manifold, this chapter proposes that the reference space be generalized to an *orbifold*, a surface with conical singularities. In contrast, recent studies on crystal growth [49] in presence of defects, the reference space, $\bar{g}_{ij}$, is modeled as non-Euclidean, i.e. $\bar{g}_{ij} \neq \delta_{ij}$, but smooth differentiable Riemannian manifold.

Homotopy theory has been used for description and classification of defects in ordered media [10]. But as noted in [10] and [50], homotopy theory fails to classify all possible distinct defects in media with broken translational order, and predicts some non-existent defect configurations. Also one needs to build a higher dimensional abstract space, *internal space/order parameter manifold* , to analyze the properties of defect. The approach taken in this chapter is akin to Volterra construction [1] (cut-deform-paste). The operations, as in Volterra construction, are done in real space. This gives an operational definition of generating topologically distinct configurations and classify them.

Poénaru [50] suggests adopting foliations, used in dynamical systems theory, to study systems with broken translational symmetry. This approach was explored in [46, 47]. Here the metric is analyzed from a quadratic differential point of view and its properties are studied to get a description of defects and textures in vector ordered medium. This chapter expounds on the analogy and similarities with dynamical systems theory to extract some useful results. Here special flat surfaces called *translation surfaces* are used to study the different configurations of the crystal.

Advantage of the formulation used in this chapter is that it is not merely classification, it also gives an operational method of constructing topologically distinct crystal configurations (such as winding number, disclination, dislocation) on surfaces of all genus. This parallels the *Volterra construction* which is used to insert defects into a continuum media, where sections of material are removed or inserted. Fig. 14 shows the process over a tubular section enclosing the defect line.

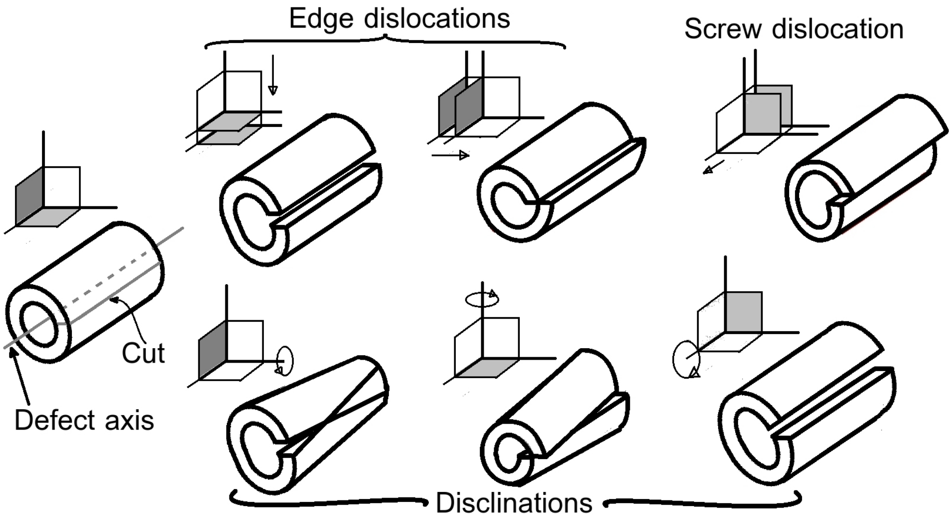

Figure 14: Volterra construction in 3d: The figure demonstrates the effect of defects presence on concentric cylindrical sections of the medium. The coordinate system on the top-left of each configuration indicates the action on the lower cut face.

Volterra construction in 2d involves removing or inserting sectors at a point. Here a dislocation can be modeled as a disclination dipole (see fig. 15). The approach described in this chapter in a way generalizes the Volterra construction.

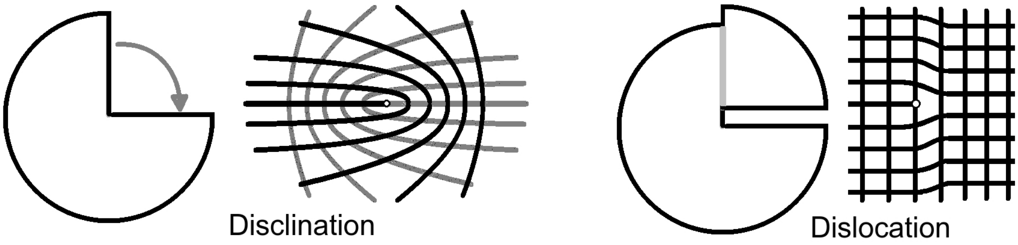

Figure 15: Volterra construction in 2d: Figure on left is the construction of a disclination and the one on right is a dislocation formed by a pair of equal and opposite disclinations.

This chapter is organized as follows: in sec. 3.2 we motivate the need to define surface with crystalline order through the gift wrapping problem and the reference space is modeled using orbifolds. Mapping class groups are used for classification of reference space based on Dehn twists. A finer classification using partial Dehn twists is provided in sec. 3.3 using translation surfaces. Further we construct a separatrix to decompose the surface into cylinders and classify them. Sec. 3.4 gives a presciption to include disclinations and dislocations. Finally all surfaces with crystalline order with half-integer strength disclinations and dislocations are completely classified by a labeled separatrix.

3.1 CRYSTALLINE ORDER ON A SURFACE

Crystal order breaks continuous translation and rotation symmetries. The continuous symmetries are reduced to discrete symmetries. Compatibility conditions constrain the type of discrete symmetries. For example, the *crystallographic restriction theorem* [51] restricts the rotational symmetries of a crystal to 2-fold, 3-fold, 4-fold, and 6-fold (quasi-crystals are not considered here).

Different possible crystal symmetries in 2d fall under the class of *Wallpaper groups*. Fig. 16 (taken from [52]) shows the 17 possible distinct groups. The discrete translation symmetry is captured by the *lattice*. A lattice is a collection of points in $\mathbb{E}^2$ that are described in 2d by

$$\vec{R} = n_1\,\vec{a}_1 + n_2\,\vec{a}_2 \tag{53}$$

$n_1, n_2 \in \mathbb{Z}$ and $\vec{a}_1, \vec{a}_2 \in \mathbb{R}^2$ are the primitive vectors. For the analysis below only the effect of breaking continuous symmetry is of concern. In what follows we use a square lattice to simplify the discussion. This doesn't lead to a loss of generality.

3.2 GIFT WRAPPING PROBLEM

To make the problem more intuitive to handle, it is rephrased as the *gift wrapping problem*.

Statement: Given: (see fig 17)

I) A 3d object to be gift wrapped, $\mathcal{O}$, with no boundaries, i.e. if Σ is the surface of $\mathcal{O}$, then $\partial\Sigma = 0$,

II) An infinite elastic sheet of gift wrapping paper, $\mathcal{U}$, with a wallpaper group ($\mathcal{G}$) on it,

with the following restrictions (fig. 18)

(a) Wrapping paper can be cut into *simply connected* (any loop in it can be shrunk to a point) pieces of any shapes and sizes. We will call each such piece a *patch*,

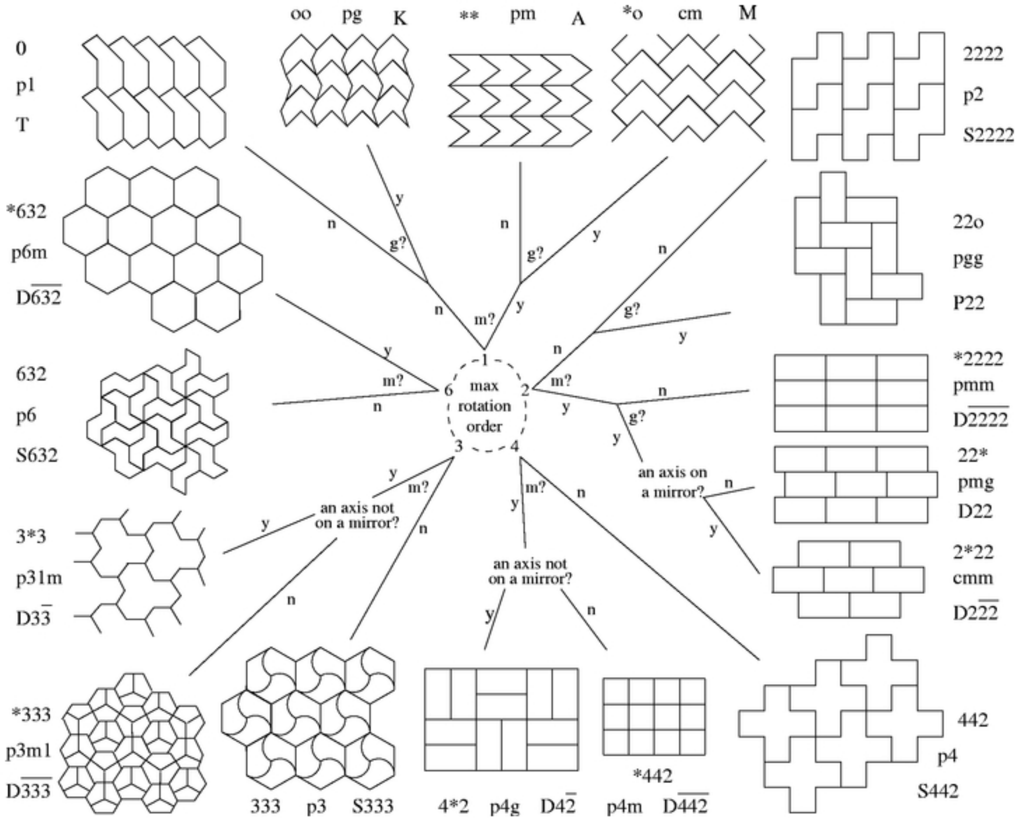

Figure 16: 17 possible wallpaper groups

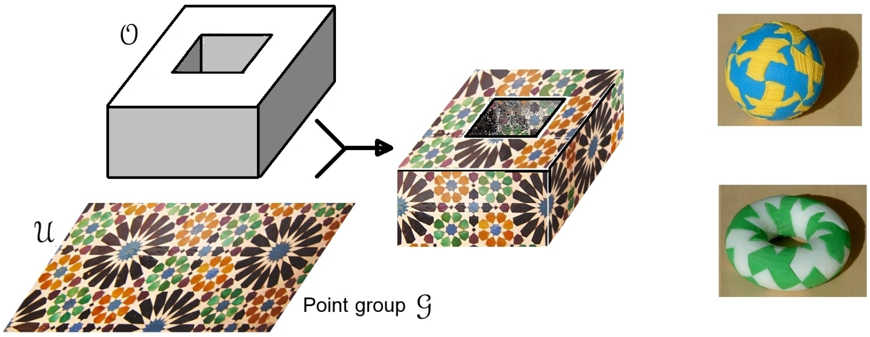

Figure 17: The wrapping problem.

(b) The paper can be stretched, compressed or sheared elastically (no tearing allowed),

(c) While wrapped, the paper should not have wrinkles and folds on the surface (one-to-one),

(d) On overlaps, the patterns must match on both patches (so that the patching process is not visible),

(e) The wrapping must cover all surface of the object, but can leave out pin holes (to accomodate defects).

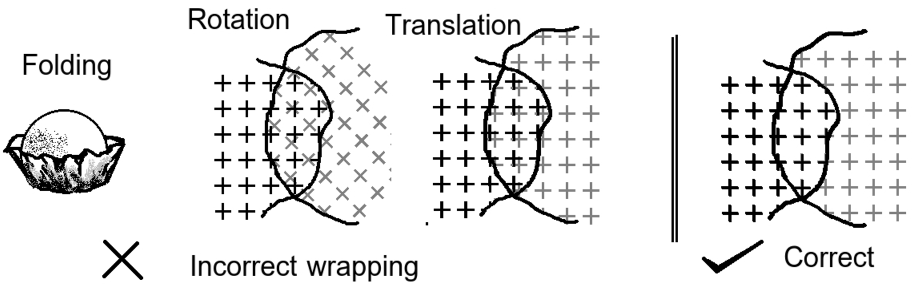

Figure 18: Schematic of wrapping rules:

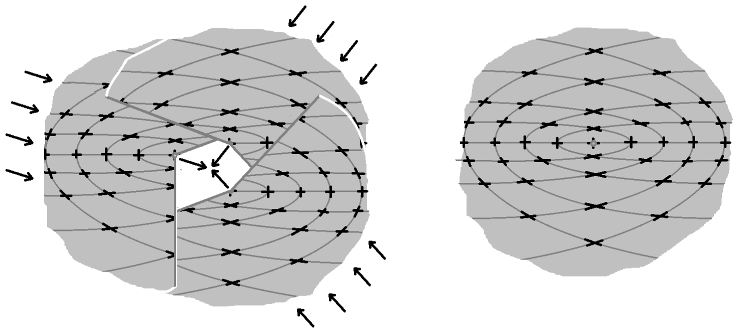

Figure 19: Figure shows how three patches of wrapping paper can be glued together such that the pattern is seamless and leaves a pin hole at the point of intesection of boundaries of all three patches. The pinhole left is the core of a $+1/2$ disclination (π rotation).

The same object can be wrapped in many different ways (wrapping is an art). Given a wrapped object, the wrap can be deformed elastically to get another wrap that looks different. However certain wraps cannot be deformed into each other via continuous deformations (see fig. 13). Note that the torus with the twist is free of topological defects such as dislocations and disclinations. This naturally leads to the following questions:

- How many such *different* wrappings are there?
- How does this number depend on the object $\mathcal{O}$ and point group $\mathcal{G}$?

In what follows we will call the gift wrapped surfaces as *surfaces with crystalline order*. Formally it is defined as

Definition : A surface Σ in $\mathbb{R}^3$ together with

I) patches $\mathcal{U}_\alpha$ which are subsets of $\mathbb{R}^2$,

II) differentiable maps $\phi_\alpha : \mathcal{U}_\alpha \to \Sigma$,

is a *surface with crystalline order* with point symmetry group $\mathcal{G}$ iff:

a) $\left\{\Sigma - \bigcup_{\alpha} \phi_{\alpha}\left(\mathcal{U}_{\alpha}\right)\right\}$ should be finitely many points (The number of pin holes should be finite),

b) The transition function, $\left(\phi_{\alpha}^{-1} \circ \phi_{\beta}\right)\big|_{\mathtt{overlap}}$, defined on the overlapping patches is discrete and belongs to $\mathcal{G}$ (see fig. 20).

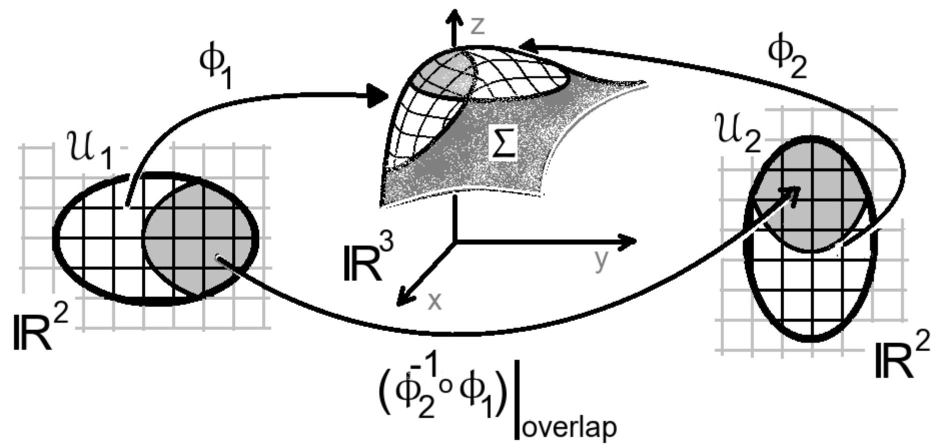

Figure 20: Charts and maps on a surface with crystalline order. Here a part of the surface sitting in 3d is covered by two patches with square lattice symmetry and a transition map of rotation by $\frac{\pi}{2}$.

As might be observed, the above definition is similar to that of a manifold. The surface with crystalline order is a finitely punctured 2d manifold with restricted discrete symmetery on the transition maps. The neighbourhood of a puncture is called *orbifold* [41], formally defined as a generalization of a manifold, wherein the space locally looks like the quotient space of a Euclidean plane under the action of the crystal point group, $\mathcal{G}$. A cone with a positive deficit angle is a canonical example of an orbifold (fig. 21). In general orbifold allows negative deficit angles as well. Thus the reference space of a crystal with disclination is an orbifold.

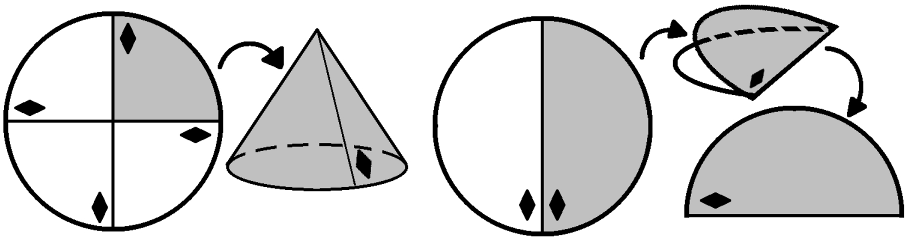

Figure 21: An orbifold formed by quotienting a plane by a discrete crystal point group is a cone. If the group is a reflection along a straight line, as in the right, then one gets a half plane with a boundary. The grey area in the plane has a one-to-one map to the orbifold.

To study the different classes of surfaces with crystalline order it is essential to consider deformations that are not smooth. One such deformation is a *Dehn twist*. Dehn twist is an operation of removing a cylindrical section from a surface, twisting it around once such that the boundaries remain the same, inserting it back into the surface. Dehn twist relatively rotates the the boundaries by 2π (see fig. 22).

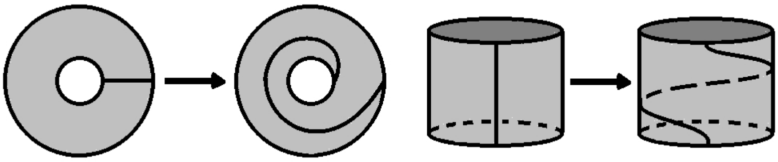

Figure 22: Figure on the right shows the operation of Dehn twist on a cylindrical section. The effect on the winding number is shown in the left figure. Observe that there are no deformations at the boundaries.

In contrast to any operations like Dehn twist, a small smooth deformation can be represented by a tangent vector field on the surface. The vector fields on $\mathcal{M}$ form a group, that is an infinite dimensional group called $\mathtt{Diff}_0(\mathcal{M})$. It is a subgroup of the *diffeomorphism group*, $\mathtt{Diff}(\mathcal{M})$, which in addition to small deformations, can also twist cylindrical sections of a surface and change the winding numbers of loops on them.

To study the full non-linear elasticity one needs to consider the whole infinite dimensional group $\mathtt{Diff}(\mathcal{M})$. Linear elasticity theory is concerned with $\mathtt{Diff}_0(\mathcal{M})$. To study the non-trivial deformations leading to twist and defects one needs to neglect or quotient out the small deformations. We therefore define *mapping class group* $\mathsf{MCG}(\mathcal{M}) := \frac{\mathtt{Diff}(\mathcal{M})}{\mathtt{Diff}_0(\mathcal{M})}$.

The theory of mapping class groups of surfaces is an active area of research in mathematics [53]. Dehn [54] showed that $\mathsf{MCG}(\mathcal{M})$ of a compact oriented surface is generated by Dehn twists on finite number of sections.

3.2.1 *Case study: Torus* $\mathsf{MCG}(\mathbb{T}^2)$

The mapping class group of a torus demonstrates the essential idea of Dehn twist and gives a concrete example for study. The plane and torus are the only topological spaces which can be covered by crystalline patches without defects or boundaries. The mapping class group of a plane is isomorphic to identity [53], hence trivial.

Torus provides the simplest non-trivial example for studying mapping class groups. One can build a defect free torus from a crystalline wrap with a single parallelogram patch, with its vertices on lattice points (see fig. 23). Using complex numbers simplifies the following analysis. The parallelogram is uniquely specified by a pair of vectors or complex numbers $\{\omega_1, \omega_2\}$, such that $\mathbb{I}\mathrm{m}\left(\frac{\omega_1}{\omega_2}\right) \neq 0$. This pair generates a set of lattice points

$$\Omega(\omega_1, \omega_2) = \{m\ \omega_1 + n\ \omega_2 |\ m,\ n \in \mathbb{Z}\}, \tag{54}$$

and the fundamental region spanned by the pair is (see fig. 23)

$$\mathcal{F}(\omega_1, \omega_2) = \{\alpha\ \omega_1 + \beta\ \omega_2 |\ \alpha,\ \beta \in [0, 1]\}. \tag{55}$$

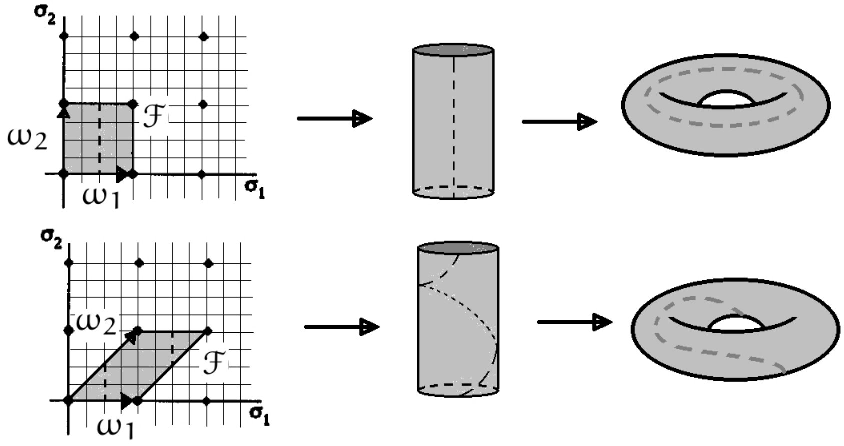

Figure 23: Generation of different surfaces with crystalline order on a torus by Dehn twist. First column shows the vectors and the fundamental regions that form the torus. Last column shows the geometrically equivalent tori with different winding numbers.

The fundamental region is rolled up and parallel sides are identified to form a torus. The same Ω can be generated by any other set of vectors related to old ones by

$$\Omega(\omega_1, \omega_2) = \Omega(\omega_1', \omega_2')$$

$$\Rightarrow \begin{pmatrix} \omega_1' \\ \omega_2' \end{pmatrix} = \begin{pmatrix} a & b \\ c & d \end{pmatrix} \begin{pmatrix} \omega_1 \\ \omega_2 \end{pmatrix}, \qquad a,\ b,\ c,\ d\ \in\ \mathbb{Z}. \tag{56}$$

To preserve the area of $\mathcal{F}$ in both basis, the determinent of the matrix should be $+1$. The above transformations form the group $SL(2, \mathbb{Z})$, *Special Linear group over* $\mathbb{Z}$, which is a set of 2×2 matrix of integers with determinent unity. Thus the mapping class group of the torus, $MCG(\mathbb{T}^2)$ is isomorphic to $SL(2, \mathbb{Z})$. The group has infinitely many elements that are generated by two transformations, namely $S : z \to -\frac{1}{z}$ and $T : z \to z + 1$, for all complex numbers z [41].

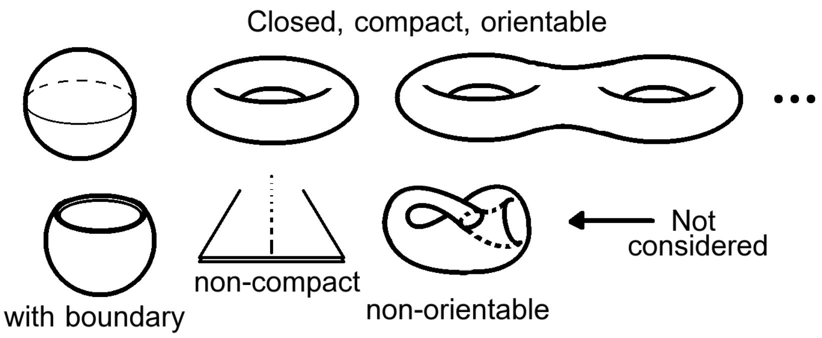

Figure 24: Different class of surfaces are shown, only surfaces in the first row are analyzed below.

3.2.2 *Higher genus compact, closed, orientable surfaces*

Since closed non-orientable surfaces are not embeddable in $\mathbb{R}^3$ they are not considered in elasticity theory. All closed, compact, orientable surfaces are topologically completely classified by the genus [41] (fig. 24). The universal procedure to obtain mapping class group using Dehn twist on a surface of any genus is discussed in the mathematics literature [53]. We just quote the results.

Theorem (Dehn-Lickorish theorem): [53] *For genus* $g \geqslant 0$, *the mapping class group* $MCG(\mathcal{M})$ *is generated by finitely many Dehn twists about nonseparating simple closed curves(A simple closed curve that doesn't split up the surface into two disconnected surfaces with boundaries, see fig. 25).*

Theorem (Lickorish generators): [53] *For genus $g \geqslant 1$, the Dehn twists about the curves* $a_1, ..., a_g, m_1, ..., m_g, c_1, ..., c_{(g-1)}$ *shown in fig. 25 generate* $MCG(\mathcal{M})$.

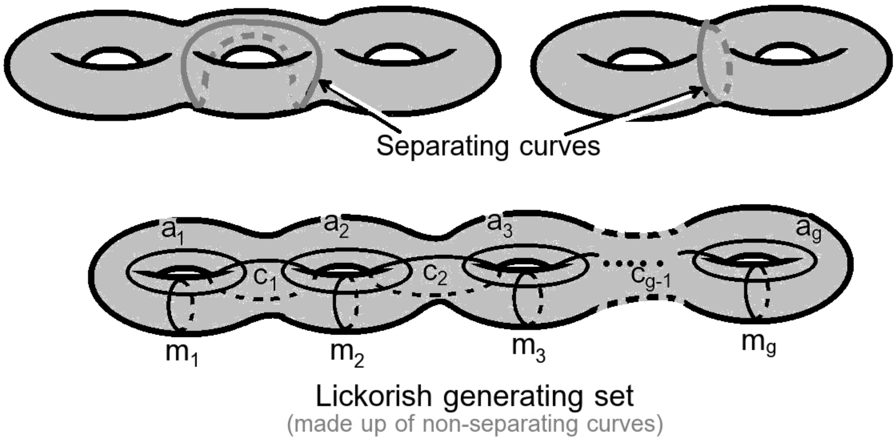

Figure 25: The figure at the top show separating curves. Bottom row shows the Lickorish generators for a surface without defects.

The closed curves/loops in the 2nd theorem specify the direction in which a cut is to be made and a cylindrical section extracted (see fig. 25). A canonical Dehn twist is applied on these sections and glued back into the surface. Point topological defects such as disclinations and dislocations are modeled as holes (called marked points in the mathematics literature [53]). In presence of defects additional curves, which are not deformable to each other have to be included in the generating set. For example a torus with a pair of disclocations shown in fig. 26 has three generators compared to two in the defect free case.

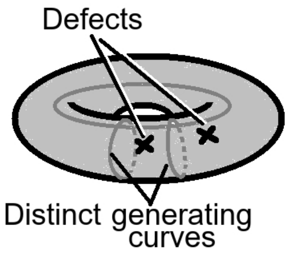

Figure 26: The three generating curves on a torus with two defects are shown. The corresponding case for a dislocation pair is discussed in sec. 3.4.0.1.

3.2.3 *Need for finer structure/classification*

$\mathrm{MCG}(\mathcal{M})$ does not fully classify and generate all the different configurations possible for the crystalline surface. The Dehn twists relatively rotated the two boundaries of the cylindrical sections by 2π. Since the crystal has a lattice, one can twist by an integer number of lattice spacings. Thus based on crystal symmetry and the boundary of the exracted cylinder, the twists can be fractions of 2π (see fig. 27).

From fig. 28 we see that the boundary curve has to be along a crystallographic axis[1] , in order to apply a partial Dehn twist. Infinitely many configurations related by smooth deformations belong to a single class of surfaces with crystalline order. These deformations change the local orientation of crystallographic axes. Thus it is best to work with the undeformed reference state $\bar{g}_{ij}$ for classifying surfaces with crystalline order. From the previous section we know that $\bar{g}_{ij}$ is flat and has conical singularities. The structure and properties of flat surfaces with isolated conical singularities are studied in dynamical systems in the context of 2d billiards table problem [20]. The geodesics on these flat surfaces are straight lines. With the identification: *geodesics on flat surfaces* $\Longleftrightarrow$ *crystallographic axes*, the properties of

---

[1] The crystallographic axes are lines along the basis vectors that we can draw in the crystal lattice. These will define a coordinate system within the crystal

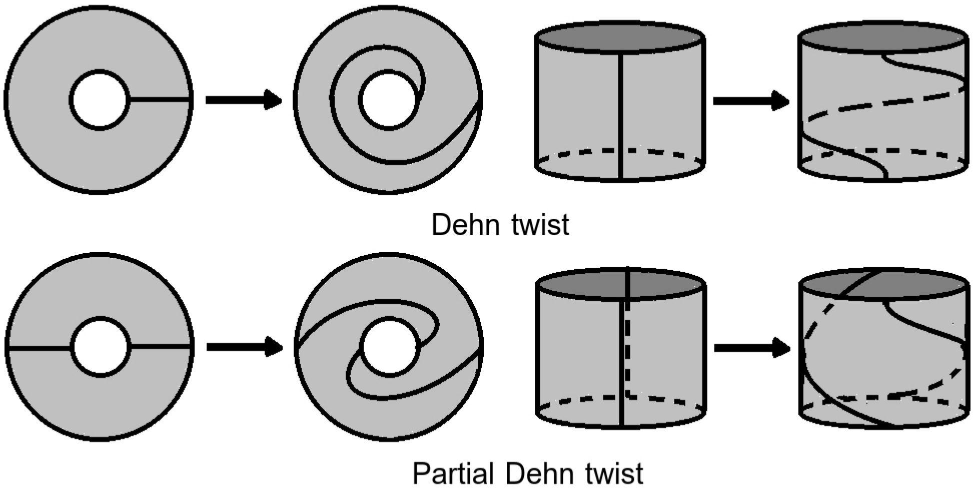

Figure 27: Comparison between full and partial Dehn twists

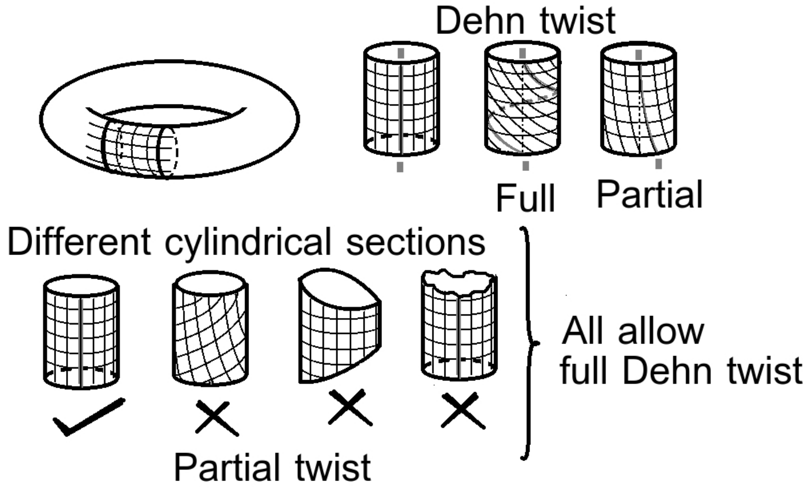

Figure 28: Problem with implementing partial Dehn twists: Since in the case of Dehn twists the boundary is not deformed the orientation of cut made to extract the cylindrical section doesn't matter. But for partial Dehn twist the cut has to be along the crystallographic axis. The cylindrical sections shown in the bottom row can undergo Dehn twists, but any partial twist will make them incompatible to insert back into the surface.

geodesics in dynamical systems can be carried over to study surfaces with crystalline order.

In the next section we discuss how any surface can be deformed to a flat surface with conical singularity.

3.3 FLAT SURFACES

The elastic deformations carried out in the previous section using $\mathtt{Diff}_0(\mathcal{M})$ are in-plane. One can also deform the surface along its normal. The $\mathrm{Diff}_0(\mathcal{M})$ acts as reparametrization of the surface and retains the Gaussian curvature K_G. Deformations along normal can change K_G. For a closed compact surface of genus g with no boundaries, the integral of K_G is related to genus g by the *Gauss-Bonnet* theorem as

$$\oint K_G \sqrt{g}\, d^2\sigma = 2\pi(2-2g). \tag{57}$$

This implies that a torus, $g = 1$, can be deformed to have zero Gaussian curvature everywhere. But a sphere or $g \geqslant 2$ surfaces cannot be deformed into those with $K_G = 0$ everywhere. A surface of genus g can be deformed into a constant Gaussian curvature surface. If $g = 0$ (sphere) the constant curvature is positive. Similarly for $g = 1$ (torus) it can have zero curvature everywhere. For genus $g \geqslant 2$, , curvature can be made -1 everywhere. This is the essence of the *Uniformization theorem*[41].

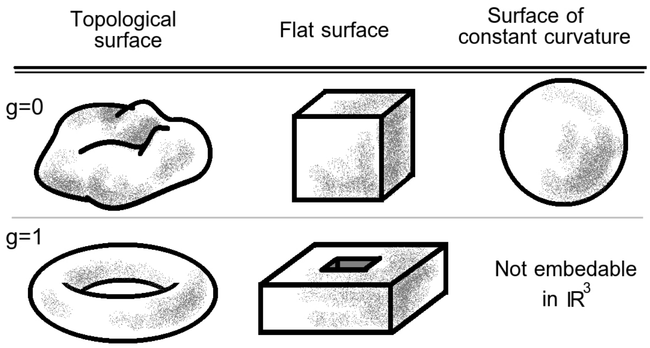

Figure 29: Flat surface and constant curvature surfaces form the extreme models analyzed in this chapter. Flat surfaces have planar faces, straight edges and isolated conical singular points and are ideal for studying the properties of geodesics.

On the other hand a sphere can be flattened to a cube (fig. 29), such that mean curvature is non-zero along the edges and Gaussian curvature, $K_G \neq 0$ only at the corners of the cube. These singular points are locally conical in shape. For a cone with deficit angle α (fig. 30),

$$\begin{aligned} \int_\Sigma K_G \sqrt{g}\, d^2\sigma &= \alpha \\ \Rightarrow K_G &= \alpha \frac{\delta^{(2)}(\vec{r}-\vec{r}_0)}{\sqrt{g}} \end{aligned} \tag{58}$$

A *flat surface* has zero Gaussian curvature everywhere except at isolated points. As mentioned in the previous section a flat surface is simpler to work with as the geodesics on any patch which does not include the conical singularity are straigth lines. These patches can

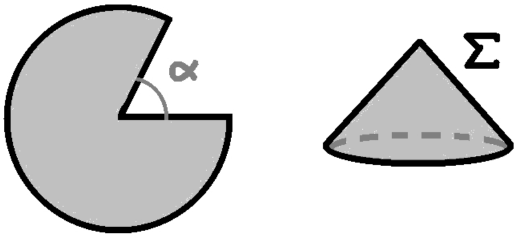

Figure 30: To construct a cone out of paper, a sector of deficit angle α is removed and the cut edges glued together. Then the cone is flat, i.e. Gaussian curvature is zero, everywhere except the apex.

be flattened into a plane without stretching. This flattening also preserves crystalline symmetries. Defects can be located at the isolated singular points.

Now if a sphere is flattened to a cube, then it has 8 singular points corresponding to its corners. Each corner has a deficit angle of $\frac{\pi}{2}$, thus a $+\frac{1}{4}$ disclination. Therefore a sphere disclinations of total strength $+2$, and a deficit angle of $+4\pi$ as expected from Gauss-Bonnet theorem (sec. 3.3). As shown in fig. 29, a genus one surface (torus) has eight $+\frac{1}{4}$ disclination on the outer corners and eight $-\frac{1}{4}$ disclination on the inside corners, which cancel each other. Hence total deficit angle for a torus is zero. Similar calculation for a genus two surface shows that there are eight more $-\frac{1}{4}$ disclinations corresponding to a total deficit angle of -4π. From the Gauss-Bonnet theorem it follows that for $g \geqslant 2$ the surface should have at least one defect.

In the next section we describe a particular representation of flat surfaces with conical singularities (translation surfaces) of any genus, that is best suited to exploit the properties of geodesics as described in the theory of dynamical systems.

3.3.1 *Translation surfaces*

In this section we describe the construction of translation surfaces. To represent the translation surface of arbitrary genus g, we proceed as follows : Let $2g$ vectors, $\vec{v}_i$ not all collinear be such that

$$\vec{v}_i = n_i\,\vec{a} + m_i\,\vec{b}, \qquad n_i, m_i \in \mathbb{Z}; \qquad i \in \{1, 2, ...2g\}$$

These vectors, as an ordered set $\{\vec{v}_1, \vec{v}_2, ...\vec{v}_{2g}\}$, define a path $\mathcal{P}$ in the lattice space (see fig. 31). Define another path $\mathcal{P}'$ with the reverse ordered set, $\{\vec{v}_{2g}, \vec{v}_{(2g-1)}, ...\vec{v}_1\}$. Both paths $\mathcal{P}$ and $\mathcal{P}'$ have same start and end points by definition. If the paths don't intersect, they form a loop enclosing a polygon, that has all its vertices lying on lattice points. Now glue/identify the sides corresponding to the pair of vectors with the same label $\vec{v}_i$ in $\mathcal{P}$ and $\mathcal{P}'$. The surface thus obtained will have genus g. This can be verified by calculating the sum of deficit angles (or interior angles) at each vertex of the patch, and using Gauss-Bonnet theorem. Thus a genus g, closed compact surface without boundary can be covered by a single patch of wrapping paper. Fig. 31 demonstrates the above construction for a genus two surface.

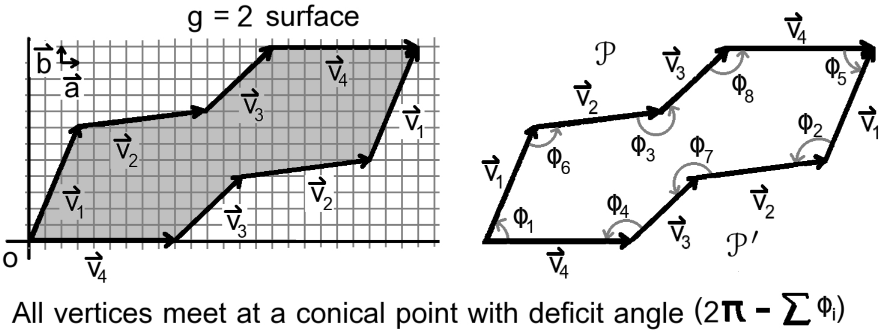

Figure 31: Construction of paths $\mathcal{P}$ and $\mathcal{P}'$ on the crystalline lattice with principal crystallographic axes along $\vec{a}$ and $\vec{b}$. The horizontal lines as well as the vertical lines of the lattice represent the geodesics. Here sum of all internal angles ϕ_i's equals $\pi(n-2)$, for an n-gon. Hence the total deficit angle and the integral of Gaussian curvature is -4π, implying it is a genus two surface by Gauss-Bonnet theorem (57).

This construction gives a closed surface with genus g and one point where all the vertices of the polygon will be glued together (see fig. 32). Hence the defect point will have an excess angle of $4\pi(g-1)$. Fig. 32 demonstrates the gluing process to get a genus two surface.

Borrowing terminology from dynamical systems [20], the horizontal geodesics (principal crystallographic directions in the crystal), as shown in fig. 33 continue to be horizontal, flow in the same direction as they cross any edge, and reemerge on the other identified edge. Hence the surface can naturally be given a global direction. The surfaces thus generated are called *translation surfaces* as the tangent vectors to the geodesics are only translated to different positions when crossing an edge. Since the geodesics are always horizontal they do not self intersect. Hence the parallel geodesics foliate the surface. The crystallographic axes, being straight lines form the periodic geodesics by construction.

We have thus succeeded in representing an arbitrary genus surface with crystalline order having integral strength (integer multiple of 2π) disclinations. In order to implement partial Dehn twist, we need to break up the translation surface into cylindrical sections. In the following section we demonstrate how this is done.

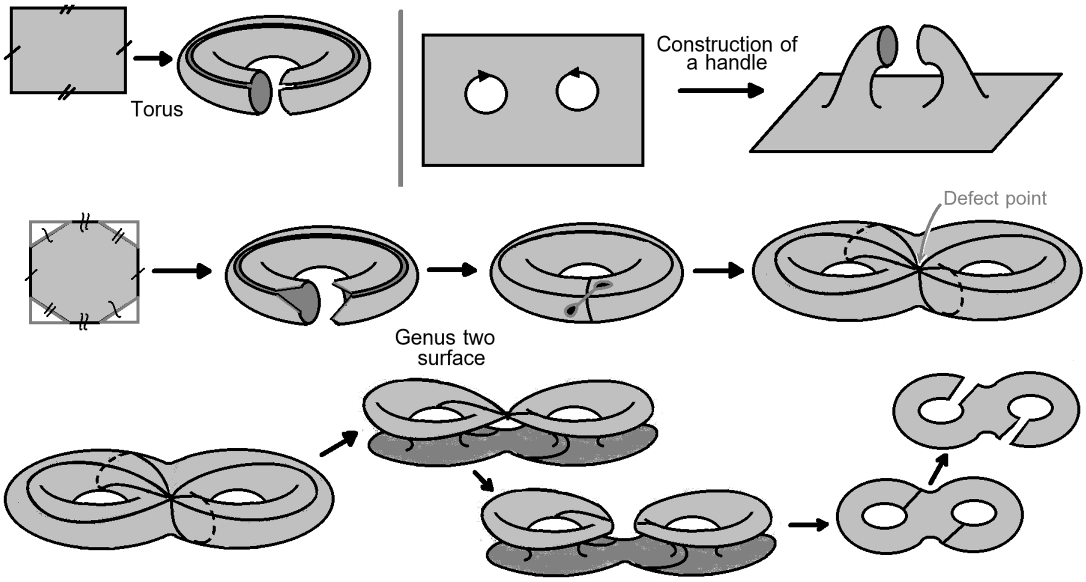

Figure 32: First row shows the construction of a torus and a handle. Second row demonstrates the sequence of operations to build a genus 2 surface. Here the sides of an octagon (similar to the one of fig. 31) with identical markings are glued together. All vertices of the octagon meet at a defect point with disclination strength -1. The last row shows how a genus two surface can be cut open and flattened out into an octagon.

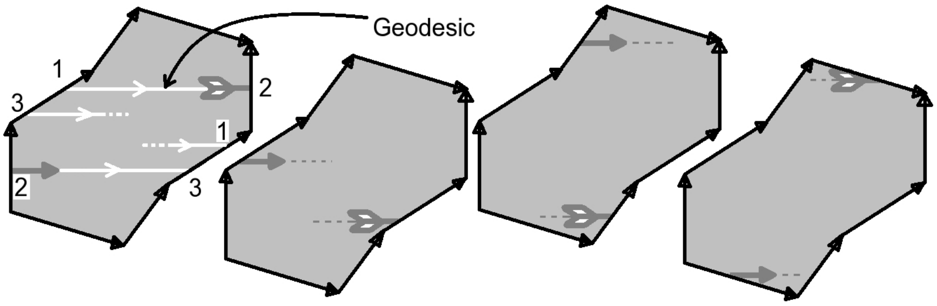

Figure 33: The exit and reemergence of horizontal lines (geodesics) into the polygon with identified (glued) edges. Being a translation surface, all geodesics continue to flow in the same direction.

3.3.2 *Decomposition of the translation surface into cylinders: Separatrix diagram*

We now give a prescription to construct a ribbon graph, called the *separatrix*, to represent a translation surface. The separatrix helps to break-up the surface into cylindrical sections on which partial Dehn twists can be applied to generate different surfaces with crystalline order.

The horizontal geodesics through the vertices of the polygon formed by $\mathcal{P}$ and $\mathcal{P}'$ are the *critical geodesics* (see fig. 34). They start and end on vertices, and hence connect two defects on the surface. We now develop each critical geodesics into ribbons by including regions on the surface in the neighborhood of the critical geodesic upto the nearest horizontal geodesics on both sides.

We now give a prescription to construct the separatrix from the polygonal translation surface with *all* critical geodesics developed into ribbons.

1. Starting from the polygonal translation surface identify the edges with similar markings. Thus we obtain the actual surface with crystalline order embedded in 3d space, with the ribbons embedded in the surface (see fig. 35).
2. Retaining only the ribbons remove all the other portions from the embedded surface to get the separatrix.

However it is difficult to draw figures for obtaining the separatrix for higher genus surfaces with defects. The alternative way to obtain the separatrix is to interchange the order of the operation described above. This alternative procedure has the further advantage that beginning with the translational polygon surface decorated with ribbons, drawn on a piece of paper, one can obtain the separatrix by cutting out ribbons with scissors and joining them by identifying similarly marked edges. The schematics in fig. 3.3.2 demonstrates the procedure.

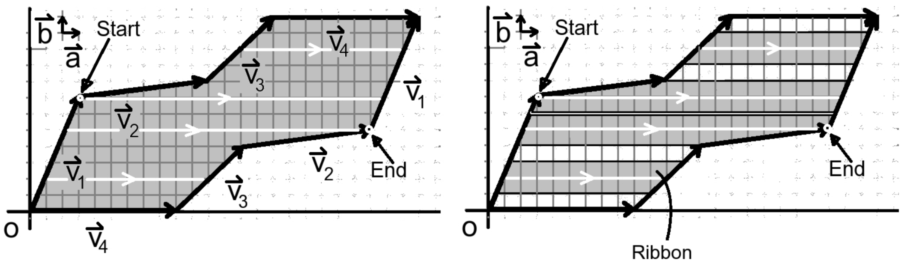

Figure 34: The trace of a horizontal critical geodesic that starts from one vertex and ends at another. There are other critical geodesics. For example the horizontal geodesic begining at the origin. This particular geodesic starts at a vertex and directly ends at a vertex. Figure on the right shows the development of a critical geodesic into a ribbon.

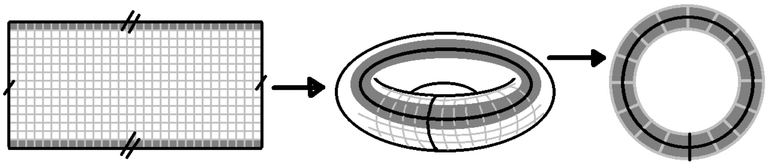

Figure 35: The ribbons on a polygonal translation surface (torus) are marked. Edges with similar markings are glued together to get the actual surface with crystalline order. Then ribbon is cut out of the surface to get the separatrix.

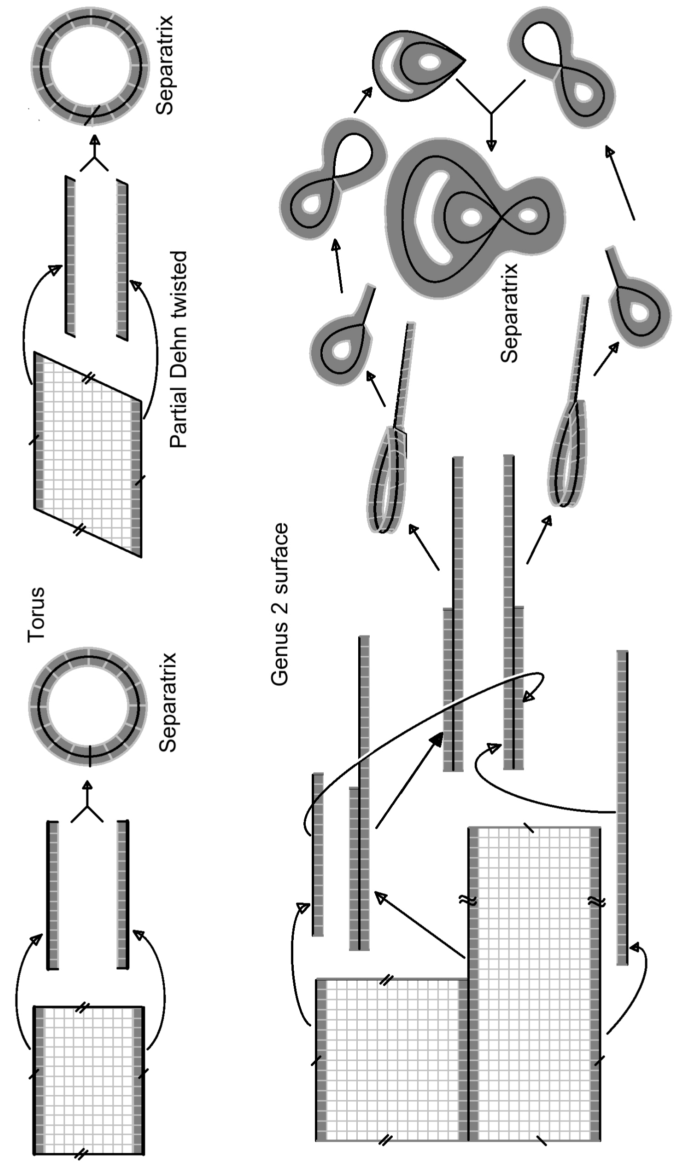

Figure 36: Top row shows the alternate construction of separatrix for a torus. The grey regions in the patch are the ribbons, that are to be cut out and glued together. Though the two tori have different crystalline order (differs by a partial Dehn twist) the separatrix are the same. It needs a label to further distinguish them. Similar construction is carried out for a genus two surface in the second row. The polygonal translation surface at the bottom for the genus two surface is an octagon, with three vertices on the bottom edge (one is hidden).

As shown in fig. 3.3.2 the ribbon edges of the separatrix of genus two surface forms loops. To reconstruct the actual surface all one has to do is connect two loops by attaching cylindrical sections (see fig. 38). Each loop in the ribbon is labeled with width, height and twist of the cylinders to be attached. The lengths are measured in terms of number of lattice points through which the geodesics pass through. Separatrix along with the labels uniquely specifies the surface with crystalline order. Fig. 37 and 38 demonstrates the labeling and reconstruction process for a genus two surface.

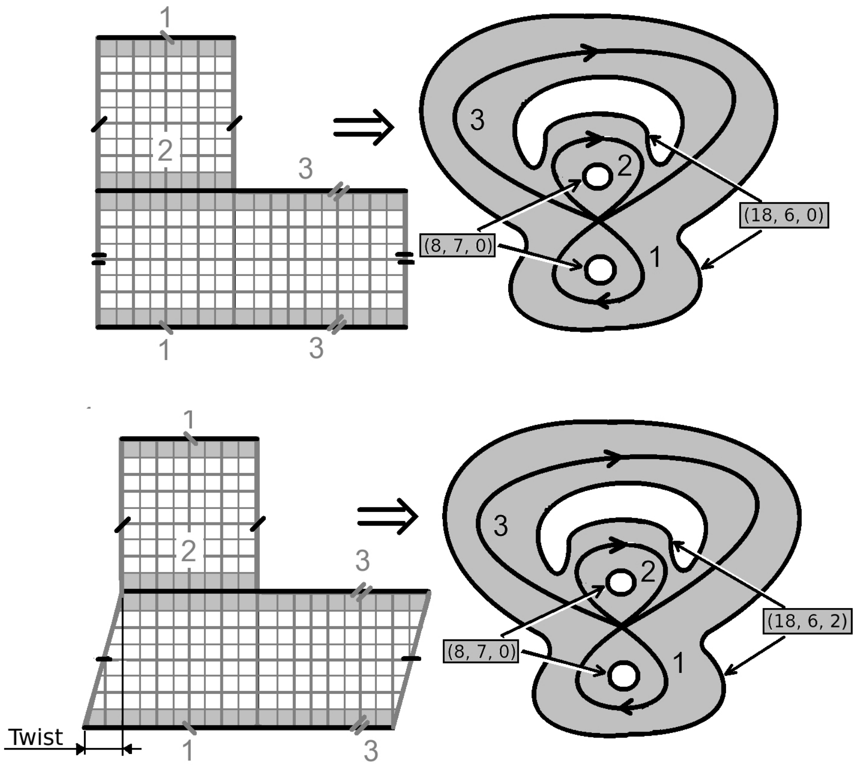

Figure 37: Example to demonstrate the labeling: Separatrix for a genus two surface which differ by a partial Dehn twist are shown. The number in box for the separatrix are the label (width, height, twist of cylinderical sections). The calculation of twist is shown in the bottom-left figure.

We have thus succeeded in classifying surface with crystalline order completely with partial Dehn twist and integer strength disclinations, using separatrix. We now move on to include fractional strength topological defects (disclinations and dislocations).

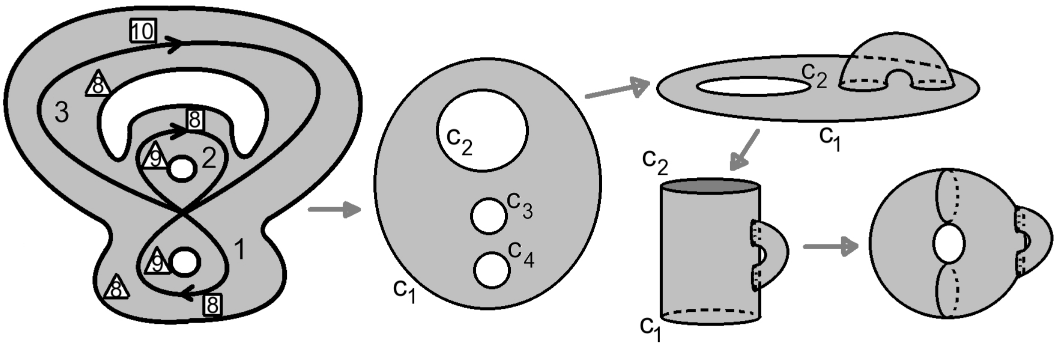

Figure 38: Reconstruction of the actual surface with crystalline order from the separatrix, by attaching cylinders. There are four loops corresponding to the separatrix on the left. Based on the labels (width, height and twist of cylinder) on the loops, cylinders are attached to get the actual surface with crystalline order. In the first step the separatrix is represented by a disc with holes having boundaries C_2, C_3, C_4. The disc has a boundary C_1. In the second step C_3 and C_4 are connected by a cylinder, whose width, height and twist are given by the label on C_3 and C_4. Same procedure is implemented on C_1 and C_2 in the last step.

3.4 INCLUSION OF HALF-INTEGER STRENGTH TOPOLOGICAL DEFECTS

Consider the modification of a flat translation surface shown in fig. 39. The construction shown in fig. 39 introduces four defects, two pairs of $+\frac{1}{2}$ and $-\frac{1}{2}$ strength disclinations at the end points of $\vec{a}$ and $\vec{b}$.

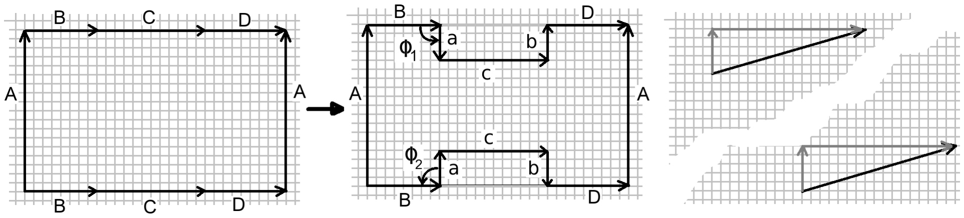

Figure 39: A torus is generated by two vectors. Disclinations are included into the torus by partitioning the horizontal vector into three vectors, $(\vec{B}, \vec{C}, \vec{D})$ and then replacing one of them, $\vec{C}$, by two vertical vectors, $(\vec{a}, \vec{b})$, and one horizontal vector, $\vec{c}$. Observe that the internal angle at the vertex corresponding to the starting point of $\vec{a}$ is $(\phi_1 + \phi_2) = \pi$, and hence a disclination of strength $+\frac{1}{2}$. The last figure shows how any vector can be decomposed into a horizontal and vertical vector, to implement the above operation of including defect. Using the above approach more defects can be introduced by partitioning horizontal vectors, $\vec{B}$, $\vec{D}$ or $\vec{c}$.

Tracing the horizontal geodesics on the polygonal surface shown in the center fig. 39, you can see that when the geodesic exits the polygon at the newly introduced vertical vectors $\vec{a}$ or $\vec{b}$, it reemerges with reversed direction (see fig. 40). The surface shown in fig. 40 is no longer a translation surface. Although the direction of geodesics are reversed, they continue to be horizontal and thus these surfaces will be refered to as *horizontal surfaces*. Note that as in translation surfaces the horizontal geodesics in horizontal surfaces either start and end on defects or close on themself, and never self intersect. Given these properties one can construct a separatrix that will decompose the surface into cylinders [55].

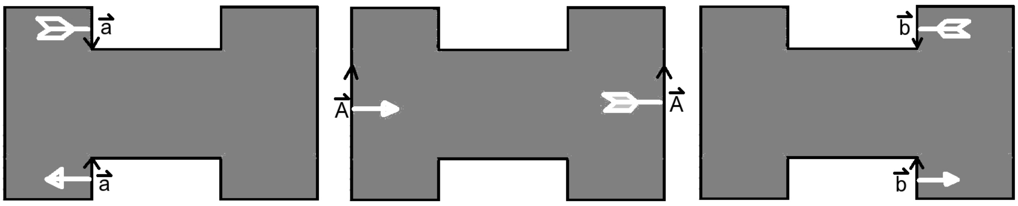

Figure 40: Schematic to demonstrate regions in a torus with defects where the geodesics change directions on crossing over an edge. First figure shows the reversal of geodesic direction on crossing $\vec{a}$ (sides of the polygon idenitified in the direction of the vector). Second figure shows that the geodesic direction is preserved on crossing $\vec{A}$. In the last figure, geodesic reverses direction on crossing $\vec{b}$.

Fig. 41 shows the construction of separatrix for an horizontal surface. The horizontal surface differs from the translation surface because the latter allows only integer strength disclinations. In the separatrix, defects sit at the vertices and its strength is indicated by the number of ribbons attached to it. If there are n ribbons at a vertex, then the deficit angle is $(2-n)\pi$, thus disclination strength is $(1-n/2)$. For a translation surface the disclination strength is always an integer, and hence will have even number of ribbons attached at each vertex. As shown in fig. 41, the horizontal surface has vertices with odd number of ribbons corresponding to half-integer strength defects.

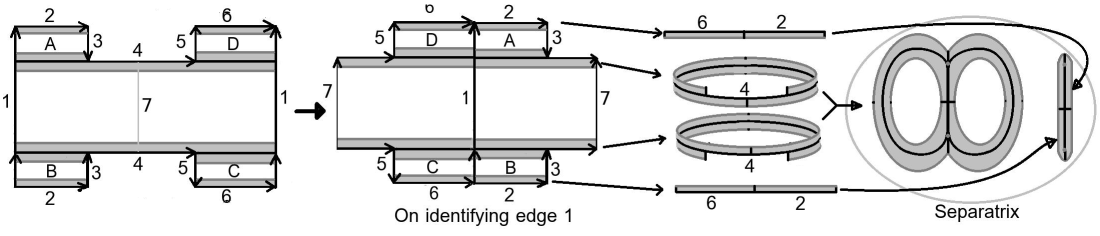

Figure 41: Construction of separatrix for a torus with ±1/2 strength disclinations. In the first step the polygonal surface is cut along middle vector 7 and rearranged as in the second figure. Then the ribbons are marked, cut out and joined together to get the separatrix. The separatrix has two disconnected parts.

3.4.0.1 *Dislocation*

In fig. 39, if the vertical vectors $\vec{a}$ and $\vec{b}$ were of half the lattice parameter, then in effect the disclinations pair-up into dipoles to form dislocations. Now the defects are no longer sitting on lattice points (see fig. 42). To build the separatrix of a polygonal surface the defects have to be repositioned on a lattice, which can be achieved by scaling all the vectors forming the polygonal surface by 2. Fig. 42 shows a torus with dislocation and its corresponding separatrix which is the same as in fig. 39, but the labels have double the values due to scaling. The fact that the defect is a dislocation will be indicated by the label (width, height, twist of the cylinder), in which the height of the cylinder connecting the two disconnected parts of the separatrix will be zero, i.e. the outer boundaries of the disconnected parts of the ribbon in fig. 42 are glued together.

Fig. 43 shows the significance of partial Dehn twist in presence of dislocation. One can see that in presence of dislocation the effect of partial Dehn twist parallels the dislocation motion known as *dislocation glide*.

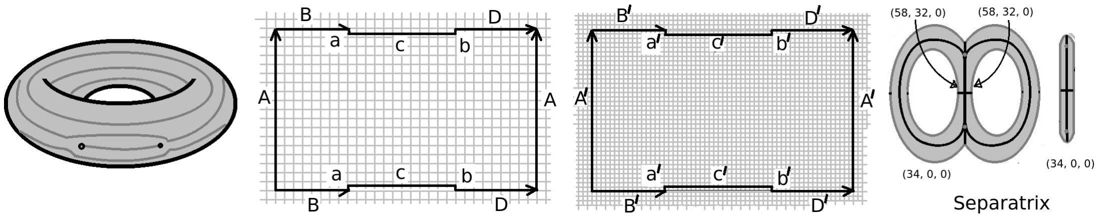

Figure 42: The disclinations in fig. 39 are transformed into dislocation by reducing magnitudes of $\vec{a}$ and $\vec{b}$ to half the lattice spacing, as in the second figure, and the vectors in this polygonal surface are scaled by 2 to get the third figure (i.e. $\vec{A}' = 2\vec{A}$ and so on). The corresponding sepratrix is shown in last figure.

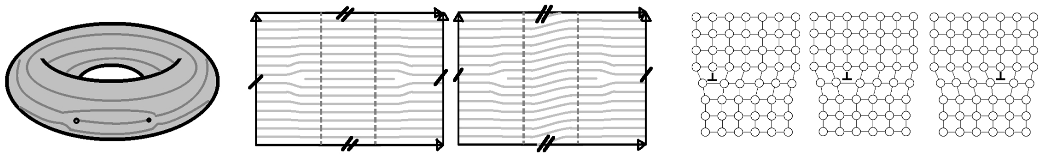

Figure 43: The effect of partial Dehn twist on the torus with dislocation is the same as plastic deformation called dislocation glide shown in the last set of figures.

3.4.0.2 *A sphere with four $+\frac{1}{2}$ disclinations: The tetrahedron model*

Consider a canonical tiling of a tetrahedron by a triangular lattice (fig: 44). Here each of the vertex has a disclination with deficit angle π. The separatrix for the tetrahedron is made up of two disconnected ribbons, with $+1/2$ disclinations sitting at each end (see fig. 44).

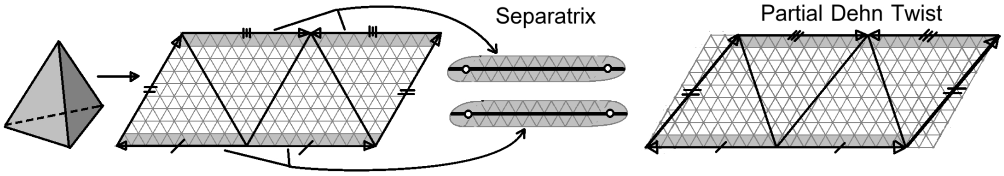

Figure 44: A tetrahedron with triangular lattice can be opened up into a parallelogram with the identifications shown. The thrid figure shows corresponding separatrix. The effect of applying partial Dehn twist is shown in the last figure.

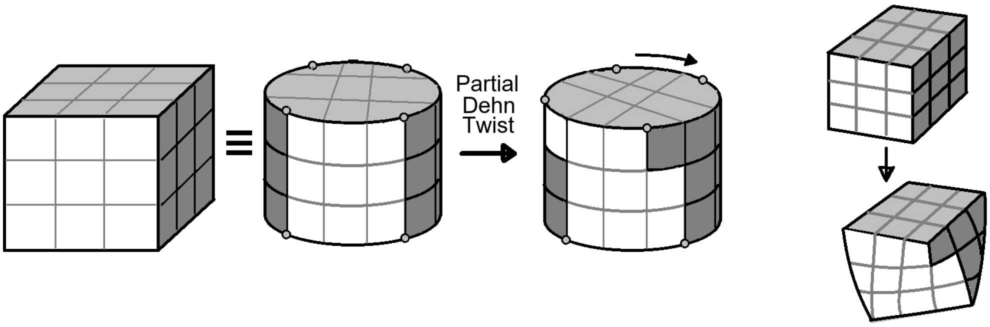

Figure 45: A Rubik's cube is equivalent to a flat sphere with eight disclinations sitting at the corners. Partial rotations of a Rubik's cube can generate crystallographically distinct set of spheres. Figure on the extreme right shows the deformed cube.

Thus in this section we have used the concepts used to study translation surfaces to construct separatrix and hence classify surfaces with crystalline order which has half-integer disclinations.

3.4.0.3 *A sphere with eight disclinations: The Rubik's cube model*

The surface of a Rubik's cube is an example of Flat surface. Each move corresponds to partial Dehn twist. If all the faces and corners (defects) of the Rubik's cube are identical then the standard moves give equivalent surfaces with crystalline order. But partial rotations, as in fig. 45, generate distinct crystal structures.

The canonical polygonal construction of cube is shown in fig. 46 (opened up box). Here one can see that the horizontal and vertical geodesics (dotted lines in fig. 46) mix. This indicates that unlike in translation or horizontal surfaces, the surface does not decompose into cylinders alone. This is because of presence of $+\frac{1}{4}$ strength disclinations. Work is in progress to further generalize the separatrix method to any fractionally charged disclinations.

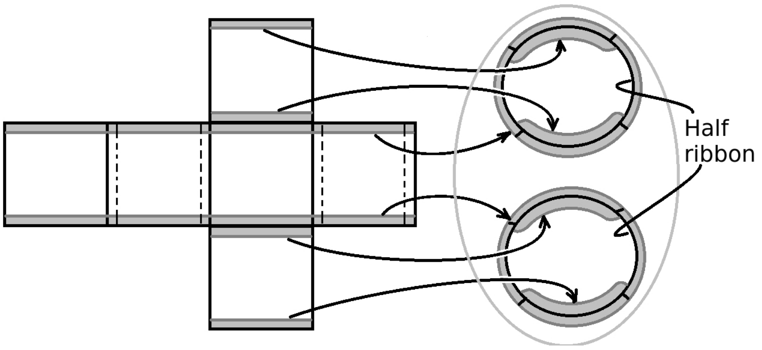

Figure 46: The cube is opened up to give a flat surface. Notice that it is not a translation surface as any horizontal geodesic in the bottom section reemerges as a vertical geodesic (dotted line) on crossing an edge. If the vertical parts are left out of the separatrix construction one gets half ribbons as shown on the right.

4

PHENOMENOLOGY OF TENT MORPHOLOGIES OF POLYMER CRYSTALLITES

In collaboration with M. Muthukumar (UMASS).

There is a significant difference between the growth of atomic crystals and polymeric crystals. Polymeric crystals have *connectedness*. This leads to interesting consequences regarding the shape and morphology of polymer crystals. In this chapter we focus on the tent morphology of polymer crystallites (see fig. 47) and suggest arguements to explain the stability of this morphology.

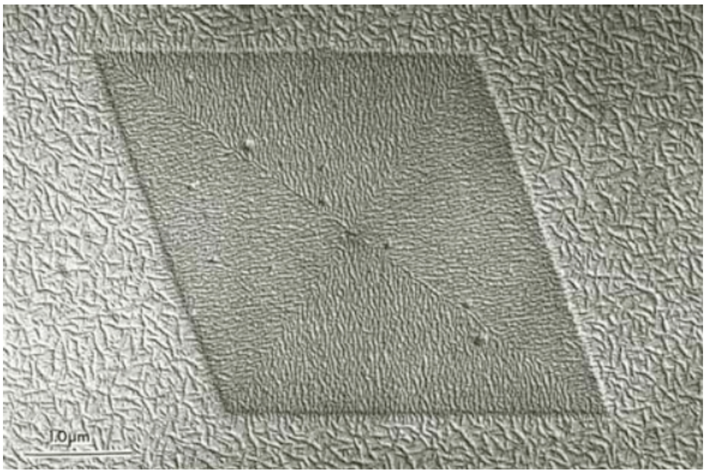

Figure 47: Polyethylene mono-crystal decorated by vacuum deposition of polyethylene. Polyethylene stripes show the four crystal growth sectors.(Copyright : J. C. Wittmann, B. A. Lotz, ICS Strasbourg)

This chapter is organized as follows: we first discuss the phenomenology and theoretical work about polymer crystallization. We then go on to discuss the connection between topological defects and the shape of the lamellar polymeric crystallites.

4.1 EXPERIMENTAL FACTS:

Very strangely all the observed morphologies of polymer crystallites are lamellar in nature. These either show spherulitic structures composed of helicoids, or tent-like structures or scroll structures [56]. As mentioned earlier polymer crystals are quite different from atomic and small-molecular crystals because polymers have the special property of connectivity. The surprising fact noticed above of finite thickness really follows from the free-energy minimization of crystallites with connectivity at non-zero temperature [57, 58]. Nevertheless within the finite thickness the typical crystal for a polyethylene is orthorhombic [59] with the polymer stem along the c-axis (see fig. 48, taken from [21]).

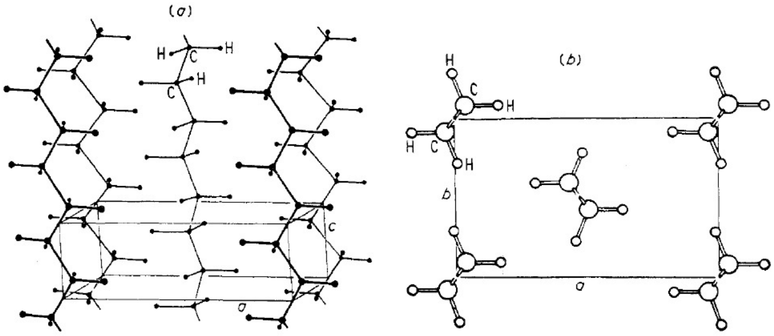

Figure 48: The crystal structure of polyethylene $([CH_2 - CH_2].)$. (a) General view. (b) Projection along chain direction.

In a melt or solution a single connected polymer need not necessarily be part of a single crystallite and can escape into melt or solution (see fig. 49, taken from [21]). The typical thickness of polyethylene lamellae is $10nm$ with polymer lengths at least ten times higher. As shown in fig. 50 (taken from [60]) the polymers fold and ren-enter the lamellae such that the surface of the lamellae are made up of folds. The minimal-energy packing of folds on the surface force the stem of the polymer to have a non-zero tilt w.r.t. the lamellar surface normal (see fig. 51, taken from [21]). This is not novel in liquid crystals. We have cases with tilt order and it is not unusual to people working in liquid crystal community [26]. But this appears in the novel context of crystallization of polymeric lamellae.

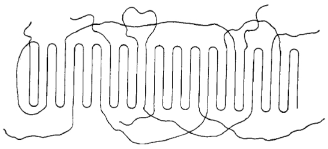

Figure 49: Schematic representation of a composite fold surface consisting of adjacently re-entrant folds and various elements of surface looseness.

Solution grown single crystals of polyethylene show tent morphologies with either four-, or six-sides. The crystallites are lamellar but not flat and have faceted boundaries (see fig. 52, taken from [61]). Atomic force microscopy studies [22] show that the folds have long range orientational order and divide the crystal into sectors. The orientations of the folds within each sector is constant and at the cross over the crystal is bent along the line separating the sectors. Experimentalist believe that " the fold direction in the single crystals is thought to be along the growth face in each sector" [61] (see fig. 52). Tent morpholo-

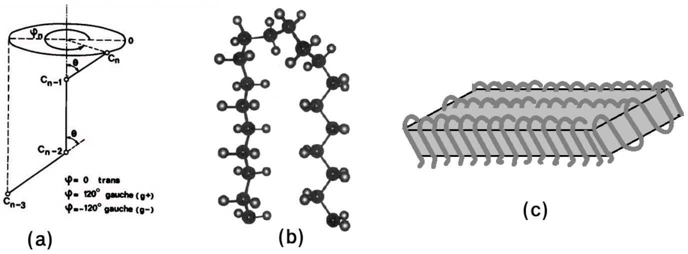

Figure 50: Polymer folding: (a) trans-gauche transitions are low energy modes that help polymers fold well below their persistence length, (b) polyethylene chain fold model used to study the free-energy of the fold surface. The fold conformation shown has six trans-gauche transitions such that the polymer re-enters the crystal in the adjacent lattice site of the lamellae. A diagrammatic representation of chain folding in polymer crystals is shown in (c).

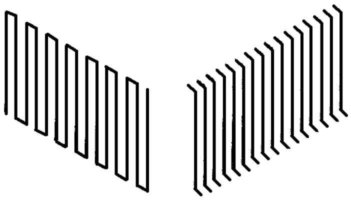

Figure 51: Sketch illustrating the tilt due to fold staggering. A single polymer has multiple folds and form ribbons. Left figure shows a ribbon of folded molecule seen normal to the ribbon plane and on the right Stacking of consecutive ribbons seen along the ribbon plane is shown.

gies of polethylene crystals can grow to tens of microns in size, and are stable over time scale of months.

With this background we have to tackle the problem of tent morphology of polymer crystallites. The problem is inherently very complicated and involves notions of physics not quite exploited in soft matter physics (see discussion in sec. 4.2.2).

4.2 PHENOMENOLOGICAL MODEL OF POLYMER CRYSTALLITES

In what follows we attempt to solve the problem of why a crystallite should buckle into the form of a tent choosing some simple notions from soft condensed matter and geometry [6]. To the extent possible we try to satisfy the full equation of equilibrium as well as the boundary conditions.

The lamellae of polymer crystals have following properties: (a) the region of finite thickness is an orthorhombic crystal and its constituent polymer chains have a tilt w.r.t. the lamella normal, (b) the surface of the lamella is covered with folds which have long-range orientational order (see fig. 52). Since the tilt is a result of fold packing (see fig. 51),

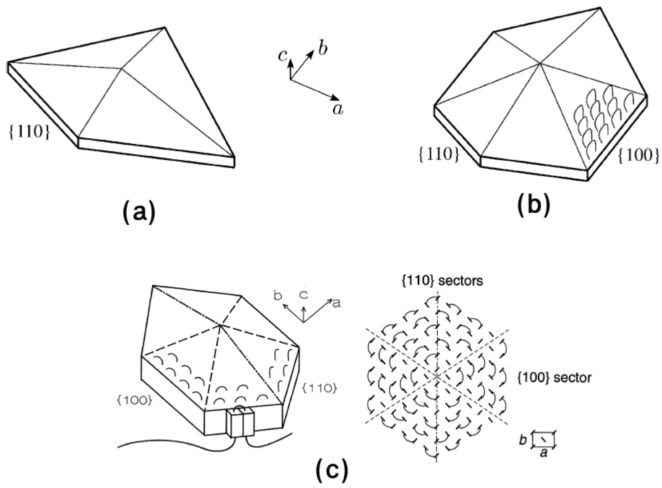

Figure 52: Schematic representations of polyethylene single crystals: (a) four-sided (lozenge-shaped) tent morphology, (b) six-sided (truncated-lozenge-shaped) tent morphology. The drawing shows the different sectors and its three dimensional shape. The fold direction for a truncated-lozenge in 3D and its top view are shown in (c). The fold directions in each sector is the same as the boundary.

both fold field and tilt field can be used interchangeably. The properties and symmetries of these systems are captured by solid phases in smectic layers with tilted molecules [62], with free energy

$$F_{ST} = \int \left(\mu\, u_{ij} u^{ij} + \frac{\lambda}{2} u^{i}{}_{j} u^{j}{}_{i} \right) dS + \int \left(\frac{K_\theta}{2} (\nabla\theta)^2 + V(\theta - \phi) \right) dS$$
$$+\, w \int (u_{ij} - \frac{1}{2} \delta_{ij} u^{k}{}_{k}) s^i s^j \, dS \,, \tag{59}$$

where μ and λ are 2D Lamé coefficients, u_{ij} is the 2D strain field, such that for a displacement field $\vec{\mathbf{u}}$

$$u_{ij} = \frac{1}{2} \left(\partial_i u_j + \partial_j u_i \right) \,, \tag{60}$$

and ϕ is the bond-orientaion angle of the 2D crystal such that the change in ϕ is related to $\vec{\mathbf{u}}$ as $\delta\phi = \nabla \times \vec{\mathbf{u}}$. The θ-field is the fold-orientation angle with $\hat{\mathbf{s}} = \{\cos(\theta - \phi), \sin(\theta - \phi)\}$. The term corresponding to w couples the fold-orientation to shear.

The potential V captures the coupling between fold- and bond- order. The point group symmetries of the 2D crystal are expressed in terms of V which breaks the local continuous rotation symmetry of the θ-field explicitly. To simplify the analysis further, we assume the 2D crystal to have square symmetry. Consider the potential V in terms of harmonics compatible with square symmetry. Let

$$V(\theta - \phi) = \frac{h_4}{4} \cos\left(4(\theta - \phi)\right) . \tag{61}$$

As discussed in the previuos section, for tent morphology, experiments suggest that the folds are oriented along the growth face. This is captured in the energetics by introducing anisotropic line tension due to folds. We neglect the anisotropy in the line tension due to the underlying bond-order of the crystal. We use the form of anisotropic line tension used to study Langmuir mono layers vector order [63]

$$F_L = \gamma \oint ds - \gamma_\theta \oint \left(\hat{\mathbf{s}}.\hat{\mathbf{t}}\right) ds \, , \tag{62}$$

where γ and γ_θ are isotropic and anisotrpic part of the line tension respectively. $\hat{\mathbf{t}}$ is the unit tangent to the boundary.

The total free-energy of a crystal with tilt order having a boundary is $F_t = F_{ST} + F_L$. In the following section, we show how anisotropic line tension due to folds leads to sector formation in the polymer crystal.

4.2.1 *Formation of sectors*

To disentangle the effects of polymer stem tilt and folds, consider a case where a polymer crystal has folds and pack together such that there is no tilt, i.e. the polymer stems are normal to the lamella surface. Then the θ- field from previous section purely corresponds to folds. Further, the analysis can be simplified by neglecting the coupling w [64]. Now the strain field and the fold-orientation field are decoupled. Variation in fold-order gives the familiar Sine-Gordon equation

$$\nabla^2\theta - \frac{h_4}{K_\theta} \sin(4(\theta - \phi)) = 0 \, . \tag{63}$$

For the case $h_4 = 0$, i.e. a fluid membrane with tilt order and anisotropic line tension, eq. (63) reduces to Laplace's equation [63]. Solving Laplace equation for arbitrary shape of the boundary is nontrivial. They work with a circle boundary, noting that experimentally observed domians are circular in shape. Analysis show that for circular domains that there exists a first-order phase transition between two distinct textures: an exterior defect (virtual boojum) texture, and an interior defect texture (see fig. 53, taken from [63]). Hence the anisotropic line tension due to tilt order traps a disclination.

We expect a similar phenomenon in solid layer with tilt-order, though the disclination/defect structure in this case is much more involved. In hexatic films with tilt order the disclinations show novel star-defect structures (see fig. 54, taken from [65]). Stability of this structure was established in [66]. The defect effectively is a disclination in hexatic- and tilt- order.

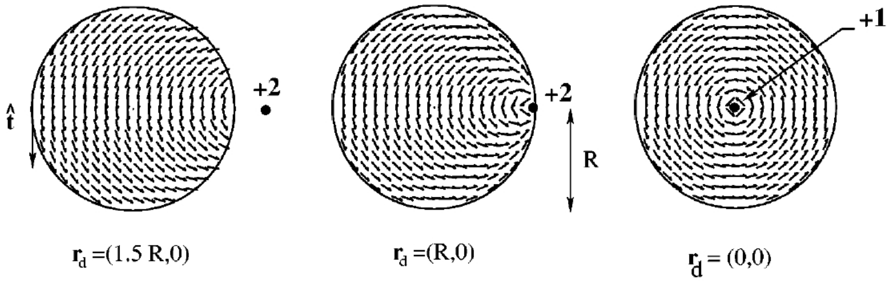

Figure 53: The ϕ field which is a solution to Laplace's equation with a point defect sitting at a distance $\vec{r}_d$ from the center of a circular domain of radius R is shown.

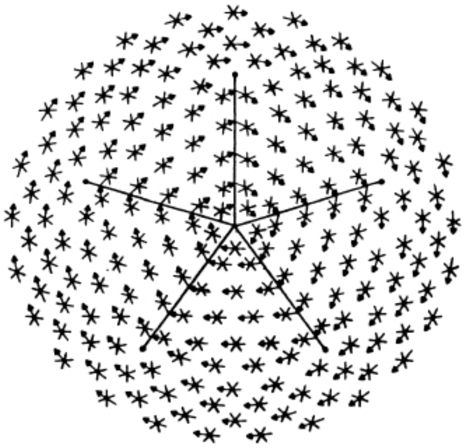

Figure 54: Calculated tilt- and hexatic-orientation pattern about the five-armed star defect. The arrows represent the local orientation of the tilt and the crosses the local orientation of the sixfold symmetric bonds (hexatic).

Here we present an exact solution to eq. (63), in the form of two orthogonal solitons, with a $+1$ disclination in θ-field on an undistorted crystal ($u_{ij} = 0, \phi = 0$),

$$\theta(x, y) = \arctan\left(\frac{\tanh(y/\omega)}{\tanh(x/\omega)}\right) + \theta_o \;, \tag{64}$$

where $\omega = \sqrt{\frac{h_4}{K_\theta}}$. A 3D plot of eq. (64) is shown in fig. 55.

As can be seen from fig. 56, the region surrounding the defect is split into four sectors. Further the anisotropic line tension due to folds, in the form of eq. (62), forces the boundary to be along the fold directions. Thus inclusion of disclination in the fold-order necessarily forces the field to have sectors and take up a boundary that is facetted.

There is no closed analytic form for the energy (eq. (59)) of the θ-field given by eq. (64). So energy for this configuration is calculated numerically. The graph in fig. 57 shows the growth in energy with the

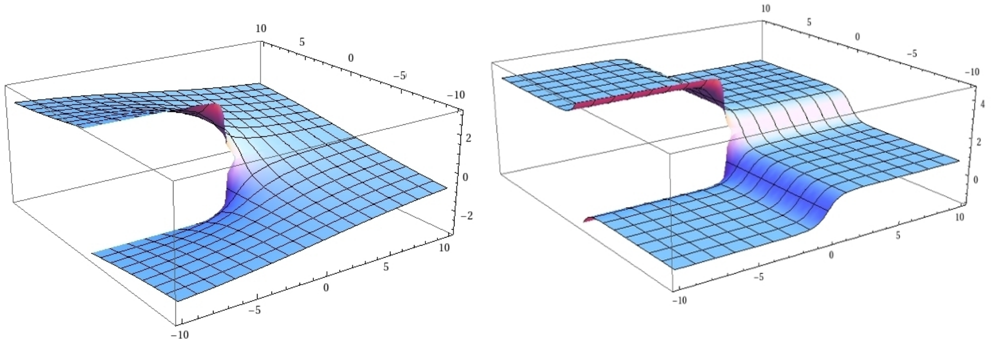

Figure 55: Comparison of θ-functions with disclination at the origin: $\theta = \arctan(y/x)$ (left) and $\theta = \arctan\left(\frac{\tanh(y/\omega)}{\tanh(x/\omega)}\right)$ (right, $\omega = 1$). The plateaus corresponding to constant orientation of θ-field can be seen on the right plot.

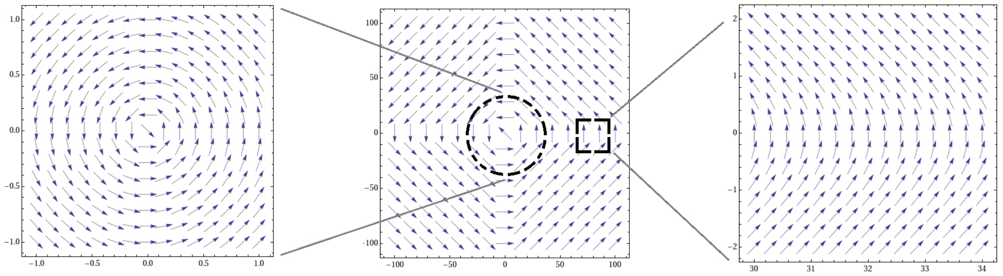

Figure 56: A plot of vector field, $\hat{\mathbf{s}} = \{\cos(\theta), \sin(\theta)\}$, corresponding to eq. 64 is shown in the center plot. Zoomed version of region close to defect core (left) shows a normal disclination like field, but assymptotically far away the solution develops a 1D wall like structure (right).

size of the crystal. The trend shows a linear increase in energy with the length of the sides.

Even though this model doesn't give the 3D structure of tent it already captures the mechanism for formation of sectors and faceted boundaries of the crystal. In next section we introduce tilt and study its effects on the crystal structure.

4.2.2 *Buckling of polymer crystal lamella*

Detailed experimental studies [67, 68, 69] have identified a mode of plastic deformations in the polymer crystal lamellae, wherein the polymer chains can slide along their axes (see fig. 58, taken from [67]). This sliding mode induces chain tilt with respect to lamella normal.

One can start by assembling a flat polymer crystal lamella with oriented folds and no tilt, and then slide the polymers along their chain axis to get the preferred tilt (see fig. 59). Thus if we start with

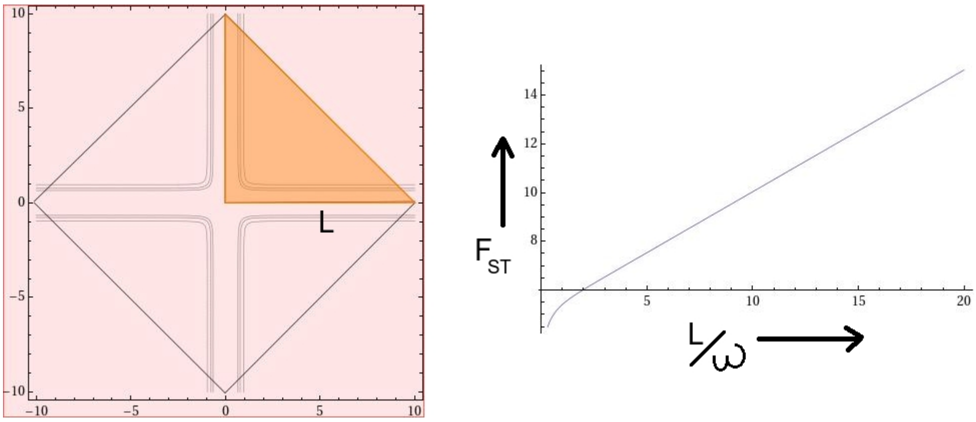

Figure 57: Figure on the left shows the approximate boundary on which the fold order is tangential. On numerical integration of F_{ST} over the region shown, of length L, we get the plot on right. For $L >> \omega$, $F_{ST} \sim L$.

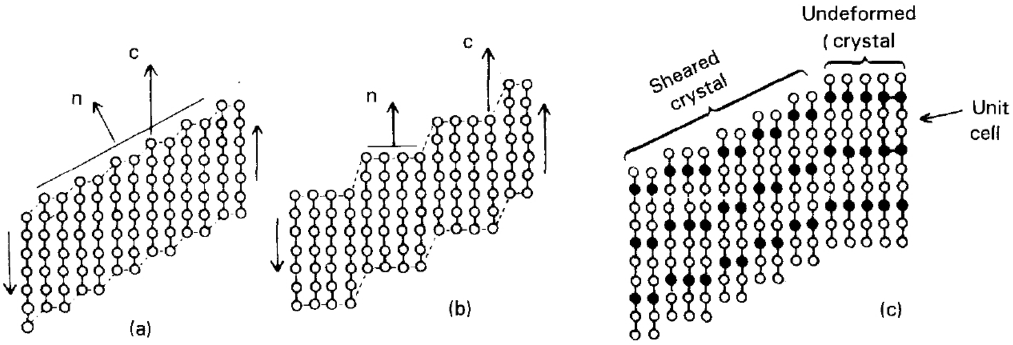

Figure 58: Schematic illustrations of different degrees of fineness of slip : (a) fine slip, (b) coarser slip, (c) shearing of a lattice that has a large lattice translation vector in the chain direction.

the fold orientation given by eq. (64), due to square crystal symmetry, inclusion of tilt forces the lamella to take on a tent structure .

The tent obtained using the above mechanism has a novel bend structure compared to usual bend in membranes (see fig. 60). The bend transformation is plastic and the curvature energy is captured by an effective h_4-term. For more details regarding the tilt-curvature coupling see B.1.

Thus far we have managed to clarify the structure and stability of the tent morphology with four sides. One can follow similar analysis to study the six sided tent, which is a result of including $\sin(2(\theta - \phi))$ term in eq. (61).

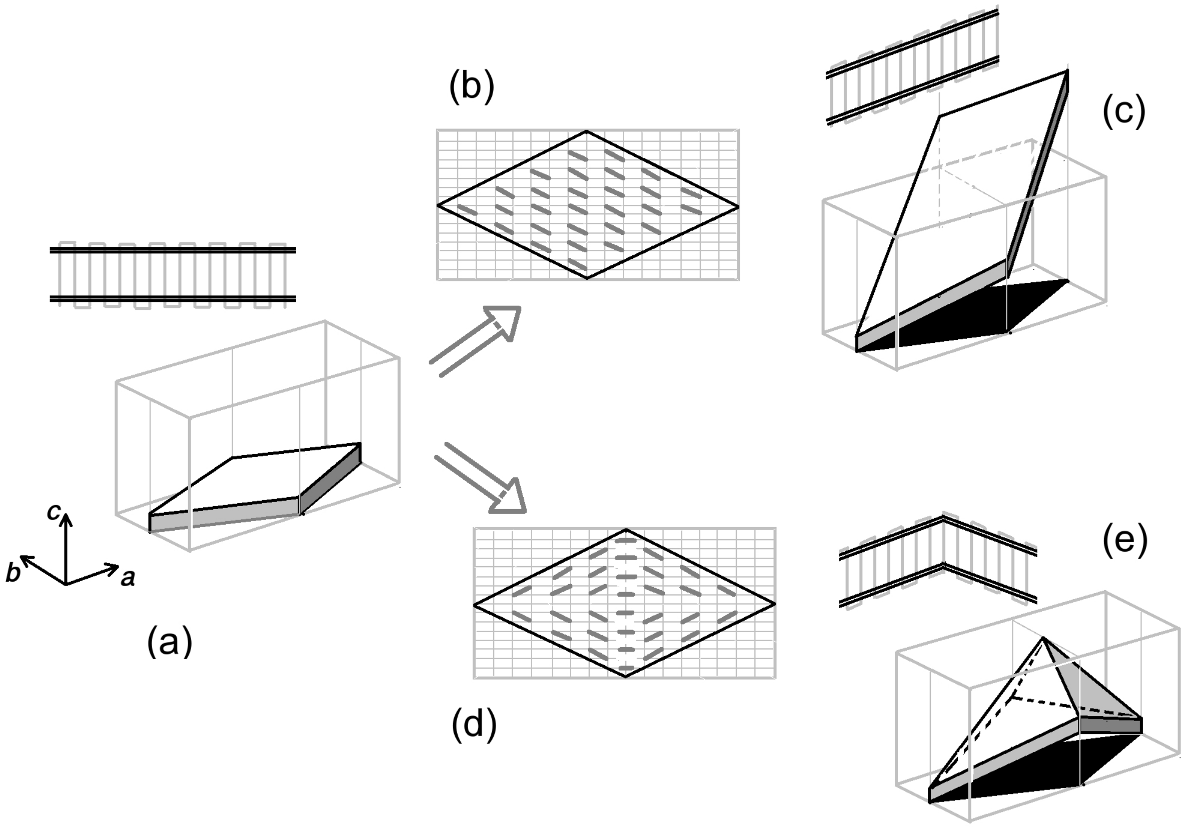

Figure 59: Buckling transition due to inclusion of tilt: (a) A flat lamella with folds but no tilt, (b) constant fold structure with no sectors which on inclusion of tilt will end up in state (c). The cross section of the lamella is shown on top of (c). Fold structure with orthogonal soliton is shown in (d) and (e) is the corresponding buckled tent-structure, along with the tilt structure of the cross-section.

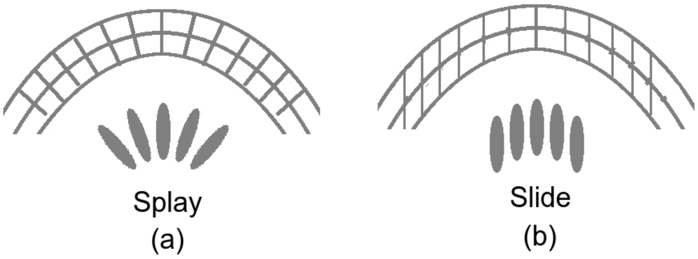

Figure 60: Bend structure: both (a) and (b) show cross section of membranes with same curvature. (a) is due to elastic deformation (splay) and (b) is due to plastic deformation (slide).

Appendices

B

ADDENDUM TO CHAPTER 4

B.1 COUPLING BETWEEN FOLD/TILT AND CURVATURE

(A) *Theory of thin plates (Föppl-von Kármán (FvK) theory)*

Large deflections in thin plates are described by 4^{th} order non-linear partial differential equations of the form [70]:

$$\frac{E\,h^3}{12(1-\nu^2)}\Delta^2 f - h\frac{\partial}{\partial x_\beta}\left(\sigma_{\alpha\beta}\frac{\partial f}{\partial x_\alpha}\right) = P, \tag{65}$$

$$\frac{\partial \sigma_{\alpha\beta}}{\partial x_\beta} = 0, \tag{66}$$

where $E \rightarrow$ Young's modulus of the (homogeneous and isotropic) plate material,
$\nu \rightarrow$ Poisson's ratio,
$h \rightarrow$ thickness of the plate,
$f \rightarrow$ out-of-plane deflection of the plate,
$P \rightarrow$ external normal force per unit area of the plate,
$\sigma_{\alpha\beta} \rightarrow$ stress tensor
$\alpha, \beta \rightarrow$ indices that take values of 1 or 2. (67)

Eq. (65) is derived by shape variation of the elastic energy

$$F_{\mathrm{plate}} = F_{\mathrm{Hooke}} + F_{\mathrm{bend}},$$

with $F_{\mathrm{Hooke}} = \int u_{\alpha\beta}\sigma^{\alpha\beta}dA$ and $F_{\mathrm{bend}} = \int \left(\frac{\kappa}{2}H^2 + \kappa_G K\right) dA$, where the integral is over the surface having mean curvature H, Gaussian curvature K, and strain tensor $u_{\alpha\beta}$. In the FvK theory of thin plates, the bend coefficients are given by [70]

$$\kappa = \frac{Eh^3}{24(1-\nu^2)} \quad \text{and} \quad \kappa_G = -\frac{Eh^3}{12(1+\nu)}, \tag{68}$$

however, see section (D) below.

(B) In addition to the above elastic free energy, we have the elastic energy of the $\hat{s}$-field

$$f_s = \frac{K_1}{2}(\nabla\cdot\hat{s})^2 + \frac{K_2}{2}(\nabla\times\hat{s})^2 \tag{69}$$

where $\hat{s} = \{\cos\theta, \sin\theta\}$, defined w.r.t. x-axis.

(C) The lowest order and most relevent coupling between deformations in the $\hat{s}$-field and curvature of the plate (lamella) is of the form

$$f_c = \eta \, H \, (\nabla \cdot \hat{s}). \tag{70}$$

(D) Canonical bending leads to splay deformation in the stems. Results of the fully covariant shape variation as well as variation in $\hat{s}$ are given in *Chapter 2*. These are nonlinear, coupled partial differential equations.

As noted in *Section 4.2.2* the bend in polymer crystal lamellae is a result of polymers sliding along their stem, with no splay. The elastic modulus κ does not correspond to the conventional bend elastic constant in standard FvK plate theory. A bend deformation of lamellar mid-plane via the sliding mode does cost energy because relative sliding of the stems changes overlap between neighbouring stems, and therefore the inter-stem interaction energy. The bend term with elastic coefficient κ that we use in F_{bend} describes the energy cost for bend from relative sliding of stems.

To make the analysis analytically tractable we assume that the lamellae are inextensible, do not employ the fully covariant theory of *Chapter 2*, and use the Monge gauge for our calculation. Note that the sliding mode preserves Monge gauge if the polymer stems are along z-axis. With these assumptions the total free energy (excluding the Gaussian curvature term, which integrates out to the boundary) is

$$\begin{aligned} F_T = \int \Big(& \frac{K_1}{2}(\nabla \cdot \hat{s})^2 + \frac{K_2}{2}(\nabla \times \hat{s})^2 + \frac{h_4}{4}\cos(4\theta) \\ & + \frac{\kappa}{2}(\nabla^2 f)^2 + \eta(\nabla^2 f)(\nabla \cdot \hat{s}) \Big) \, dx \, dy. \end{aligned} \tag{71}$$

Upon variation, $\delta F_T / \delta f = \kappa \nabla^4 f + \eta \nabla^2 (\nabla \cdot \hat{s}) = 0$. Therefore

$$\nabla^2 f = -\frac{\eta}{\kappa}(\nabla \cdot \hat{s}). \tag{72}$$

On eliminating the curvature term from eq. (71), it effectively renormalizes the coefficient K_1 to $\left(K_1 - \frac{\eta^2}{\kappa}\right) = \tilde{K}$. Within the one constant approximation, F_T reduces to

$$F_T = \int \left(\frac{\tilde{K}}{2}(\nabla^i s_j)^2 + \frac{h_4}{4}\cos(4\theta) \right) \, dx \, dy.$$

Now $(\nabla^i s_j)^2 = (\nabla \theta)^2$ [28], so the above equation reduces to eq.(63). The corresponding solution eq.(64) leads to the form of H shown in fig. 61.

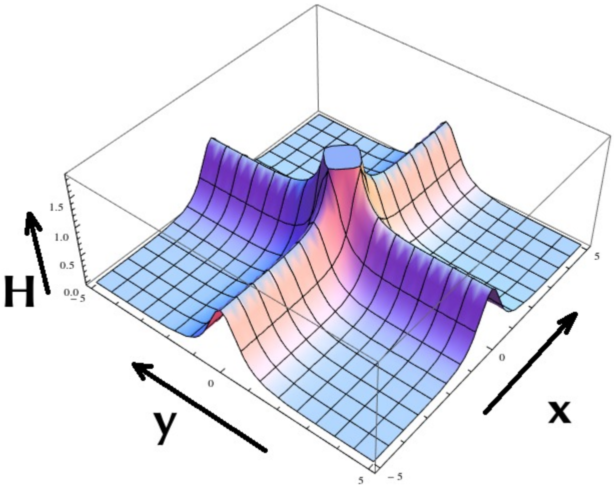

Figure 61: Mean curvature H is concentrated along two straight lines which intersect at right angles. The crystal is split into four sectors with flat regions separated by soliton walls in curvature. (Here $\frac{\tilde{K}}{h_4} = 1$).

A possible set of height functions that satisfy eq. (72) are

$$\nabla f = -\frac{\eta}{\kappa}\hat{s}. \tag{73}$$

Heuristically, using the ansatz

$$f = \alpha\ \omega \log(\cosh(x/\omega)) + \alpha\ \omega \log(\cosh(y/\omega)) \tag{74}$$

a tent like structure is obtained (see fig. 62) that satisfies eq. (73) upto a normalization function, for $\alpha = \frac{\eta}{\kappa}$ and $\omega = \sqrt{\frac{h_4}{K_\theta}}$. The phase of the normalized vector field ∇f, with f given by eq. (74), yields an exact solution for the non-linear elliptic Sine-Gordon equation (eq. (63)).

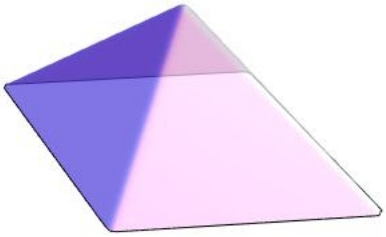

Figure 62: Plot of height function given by eq.(74)

BIBLIOGRAPHY

[1] P.M. Chaikin and T.C. Lubensky. *Principles of Condensed Matter Physics*. Cambridge University Press, 2000.

[2] A.T. Fomenko. *The Plateau Problem: Historical survey*. Studies in the development of modern mathematics. Gordon and Breach Science Publishers, 1990.

[3] R. Osserman. *A Survey of Minimal Surfaces*. Dover Phoenix editions. Dover Publications, 2002.

[4] HJ Deuling and W Helfrich. Red blood cell shapes as explained on the basis of curvature elasticity. *Biophysical journal*, 16(8):861–868, 1976.

[5] E Sackmann, J Käs, and J Rädler. On shape transformations and shape fluctuations of cellular compartments and vesicles. *Physica Scripta*, 1993(T49A):111, 1993.

[6] D. Nelson, T. Piran, and S. Weinberg. *Statistical Mechanics of Membranes and Surfaces: Jerusalem Winter School for Theoretical Physics, Jerusalem, 28 Dec. 87-6 Jan. 88*. Jerusalem Winter School for Theoretical Physics. World Scientific, 1989.

[7] W Helfrich. Elastic properties of lipid bilayers: theory and possible experiments. *Z. Naturforsch*, 28(11):693–703, 1973.

[8] Kléman, M. and Sadoc, J.F. A tentative description of the crystallography of amorphous solids. *J. Physique Lett.*, 40(21):569–574, 1979.

[9] David R. Nelson. Order, frustration, and defects in liquids and glasses. *Phys. Rev. B*, 28:5515–5535, Nov 1983.

[10] N. D. Mermin. The topological theory of defects in ordered media. *Rev. Mod. Phys.*, 51:591–648, Jul 1979.

[11] V. L. Berezinskiǐ. Destruction of Long-range Order in One-dimensional and Two-dimensional Systems having a Continuous Symmetry Group I. Classical Systems. *Soviet Journal of Experimental and Theoretical Physics*, 32:493, 1971.

[12] J M Kosterlitz and D J Thouless. Ordering, metastability and phase transitions in two-dimensional systems. *Journal of Physics C: Solid State Physics*, 6(7):1181, 1973.

[13] B. I. Halperin and David R. Nelson. Theory of two-dimensional melting. *Phys. Rev. Lett.*, 41:121–124, Jul 1978.

[14] H. S. Seung and David R. Nelson. Defects in flexible membranes with crystalline order. *Phys. Rev. A*, 38:1005–1018, Jul 1988.

[15] Jack Lidmar, Leonid Mirny, and David R. Nelson. Virus shapes and buckling transitions in spherical shells. *Phys. Rev. E*, 68:051910, Nov 2003.

[16] Carlo Carraro and David R. Nelson. Grain-boundary buckling and spin-glass models of disorder in membranes. *Phys. Rev. E*, 48:3082–3090, Oct 1993.

[17] Michael W. Deem and David R. Nelson. Free energies of isolated five- and sevenfold disclinations in hexatic membranes. *Phys. Rev. E*, 53:2551–2559, Mar 1996.

[18] Vincenzo Vitelli, J. B. Lucks, and D. R. Nelson. Crystallography on curved surfaces. *Proceedings of the National Academy of Sciences*, 103(33):12323–12328, 2006.

[19] John R. Frank and Mehran Kardar. Defects in nematic membranes can buckle into pseudospheres. *Phys. Rev. E*, 77:041705, Apr 2008.

[20] A. Zorich. Flat Surfaces. *ArXiv Mathematics e-prints*, September 2006.

[21] A Keller. Polymer crystals. *Reports on Progress in Physics*, 31(2):623, 1968.

[22] Akihiko Toda, Mari Okamura, Masamichi Hikosaka, and Yoshitsugu Nakagawa. Three-dimensional shape of polyethylene single crystals grown from dilute solutions and from the melt. *Polymer*, 46(20):8708–8716, 2005.

[23] W. Sung and P. J. Park. Polymer translocation through a pore in a membrane. *Phys. Rev. Lett.*, 77:783–786, Jul 1996.

[24] Thomas Powers and Philip Nelson. Fluctuating membranes with tilt order. *J. Phys. II France*, 5(11):1671–1678, 1995.

[25] R. Capovilla, J. Guven, and J. A. Santiago. Lipid membranes with an edge. *Phys. Rev. E*, 66:021607, Aug 2002.

[26] P.G. de Gennes. *The physics of liquid crystals*. International series of monographs on physics. Clarendon Press, 1974.

[27] H. Weyl. Elektron und Gravitation. I. *Zeitschrift fur Physik*, 56:330–352, May 1929.

[28] Nelson, D.R. and Peliti, L. Fluctuations in membranes with crystalline and hexatic order. *J. Phys. France*, 48(7):1085–1092, 1987.

[29] B.F. Schutz. *Geometrical Methods of Mathematical Physics*. Cambridge University Press, 1980.

[30] J.S. Schwinger. *Particles, Sources, and Fields*. Number v. 1 in Advanced book classics. Advanced Book Program, Perseus Books, 1998.

[31] Luca Giomi. Hyperbolic interfaces. *Phys. Rev. Lett.*, 109:136101, Sep 2012.

[32] L. Lejček. Note on the dispiration and 2Ï-disclination interaction in sm c* phases of liquid crystal. *Czechoslovak Journal of Physics B*, 35(7):726–733, 1985.

[33] L. Lejček. Twist-edge dispiration system in a finite sample of antiferroelectric liquid crystals. *Czechoslovak Journal of Physics*, 52(7):865–876, 2002.

[34] L. Giomi and M.J. Bowick. Elastic theory of defects in toroidal crystals. *The European Physical Journal E*, 27(3):275–296, 2008.

[35] www.nano-enhanced-wholesale-technologies.com/faq/carbon-forms.htm.

[36] S. Dresselhaus, G. Dresselhaus, and P. Avouris. *Carbon Nanotubes: Synthesis, Structure, Properties, and Applications*. Physics and astronomy online library. Springer, 2001.

[37] M.S. Dresselhaus, G. Dresselhaus, and R. Saito. Physics of carbon nanotubes. *Carbon*, 33(7):883 – 891, 1995. Nanotubes.

[38] J. Liu, H. Dai, J. H. Hafner, D. T. Colbert, and R. E. Smalley. Fullerene 'crop circles'. , 385:780–781, February 1997.

[39] Lei Liu, G. Y. Guo, C. S. Jayanthi, and S. Y. Wu. Colossal paramagnetic moments in metallic carbon nanotori. *Phys. Rev. Lett.*, 88:217206, May 2002.

[40] Humberto Terrones and Mauricio Terrones. Curved nanostructured materials. *New Journal of Physics*, 5(1):126, 2003.

[41] M. Nakahara. *Geometry, Topology and Physics, Second Edition*. Graduate student series in physics. Taylor & Francis, 2003.

[42] Robin Hartshorne. *Algebraic geometry*. Springer-Verlag, New York, 1977. Graduate Texts in Mathematics, No. 52.

[43] George Springer. *Introduction to Riemann Surfaces*. American Mathematical Society, 2001.

[44] Charles Nash. *Differential topology and quantum field theory*. Academic Press, London, 1991.

[45] Dale Husemoller. *Elliptic curves*. Graduate texts in mathematics. Springer, New York, 2004.

[46] Arkady L. Kholodenko. Use of quadratic differentials for description of defects and textures in liquid crystals and 2 + 1 gravity. *Journal of Geometry and Physics*, 33(1â2):59 – 102, 2000.

[47] Arkady L. Kholodenko. Use of meanders and train tracks for description of defects and textures in liquid crystals and 2 + 1 gravity. *Journal of Geometry and Physics*, 33(1â2):23 – 58, 2000.

[48] Jack Lidmar, Leonid Mirny, and David R. Nelson. Virus shapes and buckling transitions in spherical shells. *Phys. Rev. E*, 68:051910, Nov 2003.

[49] Efi Efrati, Eran Sharon, and Raz Kupferman. Non-euclidean plates and shells. 2010.

[50] V. Poénaru. Some aspects of the theory of defects of ordered media and gauge fields related to foliations. *Communications in Mathematical Physics*, 80(1):127–136, 1981.

[51] Stephen Elliott and S.R. Elliott. *The physics and chemistry of solids*. J. Wiley, 1998.

[52] Sanderson. http://www.math.toronto.edu/ drorbn/-gallery/symmetry/tilings /sanderson/index.html.

[53] B. Farb and D. Margalit. *A Primer on Mapping Class Groups (PMS-49)*. Princeton Mathematical Series. Princeton University Press, 2011.

[54] M. Dehn. Die gruppe der abbildungsklassen. *Acta Mathematica*, 69(1):135–206, 1938.

[55] Maxim Kontsevich and Anton Zorich. Connected components of the moduli spaces of abelian differentials with prescribed singularities. *Inventiones mathematicae*, 153(3):631–678, 2003.

[56] Bernard Lotz and Stephen Z.D. Cheng. A critical assessment of unbalanced surface stresses as the mechanical origin of twisting and scrolling of polymer crystals. *Polymer*, 46(3):577 – 610, 2005.

[57] P. Welch and M. Muthukumar. Molecular mechanisms of polymer crystallization from solution. *Phys. Rev. Lett.*, 87:218302, Nov 2001.

[58] Murugappan Muthukumar. Shifting paradigms in polymer crystallization. In GÃŒnter Reiter and GertR. Strobl, editors, *Progress in Understanding of Polymer Crystallization*, volume 714 of *Lecture Notes in Physics*, pages 1–18. Springer Berlin Heidelberg, 2007.

[59] C. W. Bunn. The crystal structure of long-chain normal paraffin hydrocarbons. the "shape" of the <ch2 group. *Trans. Faraday Soc.*, 35:482–491, 1939.

[60] S. P. Chum, G. W. Knight, J. M. Ruiz, and P. J. Phillips. Computer modeling of 110 adjacent reentry of polyethylene molecules. *Macromolecules*, 27(3):656–659, 1994.

[61] Yoshitsugu Nakagawa, Hitomi Hayashi, Takayuki Takahagi, Fusami Soeda, Akira Ishitani, Akihiko Toda, and Hideki Miyaji. Atomic force microscopy of solution grown polyethylene single crystals. *Japanese journal of applied physics*, 33(6S):3771, 1994.

[62] David R. Nelson and B. I. Halperin. Solid and fluid phases in smectic layers with tilted molecules. *Phys. Rev. B*, 21:5312–5329, Jun 1980.

[63] David Pettey and T. C. Lubensky. Stability of texture and shape of circular domains of langmuir monolayers. *Phys. Rev. E*, 59:1834–1845, Feb 1999.

[64] Jorge V. José, Leo P. Kadanoff, Scott Kirkpatrick, and David R. Nelson. Renormalization, vortices, and symmetry-breaking perturbations in the two-dimensional planar model. *Phys. Rev. B*, 16:1217–1241, Aug 1977.

[65] S. B. Dierker, R. Pindak, and R. B. Meyer. Consequences of bond-orientational order on the macroscopic orientation patterns of thin tilted hexatic liquid-crystal films. *Phys. Rev. Lett.*, 56:1819–1822, Apr 1986.

[66] Jonathan V. Selinger and David R. Nelson. Theory of transitions among tilted hexatic phases in liquid crystals. *Phys. Rev. A*, 39:3135–3147, Mar 1989.

[67] L. Lin and A.S. Argon. Structure and plastic deformation of polyethylene. *Journal of Materials Science*, 29(2):294–323, 1994.

[68] A. Galeski, Z. Bartczak, A. S. Argon, and R. E. Cohen. Morphological alterations during texture-producing plastic plane strain compression of high-density polyethylene. *Macromolecules*, 25(21):5705–5718, 1992.

[69] I.L. Hay and A. Keller. Polymer deformation in terms of spherulites. *Kolloid-Zeitschrift und Zeitschrift fÃŒr Polymere*, 204(1-2):43–74, 1965.

[70] L.D. Landau, E.M. Lifshitïž sïž¡, A.M. Kosevich, and Pitaevskiĭ. *Theory of Elasticity*.

COLOPHON

This document was typeset using the typographical look-and-feel `classicthesis` developed by André Miede. The style was inspired by Robert Bringhurst's seminal book on typography *"The Elements of Typographic Style"*. `classicthesis` is available for both LaTeX and LyX:

`http://code.google.com/p/classicthesis/`